Remote Sensing of Environment 322 (2025) 114696

Contents lists available at ScienceDirect

Remote Sensing of Environment

journal homepage: www.elsevier.com/locate/rse

Unveiling coastal change across the Arctic with full Landsat collections and data fusion

Tua Nylén [a,b,*], Mikel Calle [a,c,1], Carlos Gonzales-Inca [a]

[a] Department of Geography and Geology, University of Turku, Turku FI-20014, Finland
[b] Department of Geosciences and Geography, University of Helsinki, Helsinki FI-00014, Finland
[c] Turku Collegium for Sciences, Medicine and Technology (TCSMT), University of Turku, Turku FI-20014, Finland

ARTICLE INFO

Keywords:
Circumpolar
Data fusion
NDWI
Random Forest
Google Earth Engine
Coastal erosion
Change detection

ABSTRACT

Arctic communities urgently need regional to local-scale information on the rapid coastal changes, caused by thawing permafrost, melting glaciers, and declining sea ice. We introduce a procedure for mapping coastal land cover change from satellite images in the challenging Arctic conditions (and beyond). Our approach utilizes data fusion and cloud computing in Google Earth Engine to process the full Landsat collections for the entire Arctic. It merges information from multiple Landsat sensors and utilizes complementary spatial data and two algorithms to enhance classification accuracy and processing efficiency. This mitigates issues with local illumination conditions and the low availability and quality of satellite data in the Arctic before 2010s. Calculating post-classification composites of coastal land cover over five-year time-steps effectively reduces the impacts of clouds, suspended sediment, and the tide. The procedure was iteratively developed in calibration sites with contrasting physical characteristics. Validation of the final product indicates an overall classification accuracy of more than 98 % (against manually labelled data) and a median shoreline error distance of c. 20 and 10 m in mesotidal and microtidal coasts, respectively. The resulting Arctic Coastal Change dataset presents coastal dynamics from 1984 to 2023 at a 30-m resolution, and highlights hotspots that experience coastal erosion or accretion at a rate of more than 10 m/a. The overall coherence of our results with 61 other studies across the Arctic shows the robustness of the procedure. However, exploring the dataset may uncover localized errors that call for procedure improvements through new collaborative Arctic coastal dynamics studies.

1. Introduction

Largest rises in surface temperatures since the beginning of the 20th century have been observed in the Arctic (e.g., Serreze and Barry, 2011; Previdi et al., 2021; Davy and Griewank, 2023), making the coast particularly prone to shoreline displacement (e.g., Irrgang et al., 2022). Increased coastal instability is one of the most significant impacts of climate change on the local communities of the Arctic (Barnhart et al., 2014; Radosavljevic et al., 2016; Irrgang et al., 2019). Shoreline displacement has severe consequences for land use, i.e., human settlement, traditional exploitation of raw materials, transport, and cultural heritage (AMAP, 2019; Irrgang et al., 2019).

Thawing of the permafrost-rich riverbanks decreases their stability (Rowland et al., 2023), and increasing meltwater runoff from glacial watersheds (e.g., Valentin et al., 2018) brings more sediments into the coastal system, causing seaward displacement of the shoreline around those estuaries (e.g., Bourriquen et al., 2016; Lepkowska and Stachnik, 2018; Tallentire et al., 2023). Decreased sea ice and fast ice cover and shortening ice period increase wave action and length of the open water period, leading to accelerated erosion of the coast (Overeem et al., 2011; Barnhart et al., 2014; Nielsen et al., 2020; Luetzenburg et al., 2023). Thawing of the permafrost-rich coasts decreases their stability and makes the shoreline more prone to erosion (Lantuit and Pollard, 2008; Gibbs et al., 2021). Permafrost thaw also causes ground subsidence relative to sea level, leading to shoreline retreat (Wang et al., 2023). In many parts of the Arctic, post-glacial land uplift still compensates for the global sea level rise and causes shoreline advancement.

These processes operate at different spatial and temporal scales and are further impacted by local environmental conditions (Bendixen and Kroon, 2017; Farquharson et al., 2018). Thus, shoreline displacement is

* Corresponding author at: Department of Geography and Geology, University of Turku, Turku FI-20014, Finland.
E-mail addresses: tua.nylen@utu.fi (T. Nylén), mikelcal@ucm.es (M. Calle), cagoin@utu.fi (C. Gonzales-Inca).
[1] Present address: Universidad Complutense de Madrid, Avda. de Séneca 2, Ciudad Universitaria, 28040 Madrid, Spain

https://doi.org/10.1016/j.rse.2025.114696
Received 29 November 2024; Received in revised form 4 March 2025; Accepted 4 March 2025
Available online 11 March 2025

associated with large and potentially unforeseeable local variation (Are et al., 2008; Bendixen and Kroon, 2017; Overeem et al., 2022). Since the intensity of coastal changes will vary locally, also the impacts on local communities and the local economy will be highly variable. This kind of spatially varying change is usually impossible to measure with discrete or point observations and requires continuous spatial data.

Previous studies have quantified local and regional-scale shoreline displacement rates using remote sensing, which compensates for the lack of direct measurements of shoreline positions (Lantuit et al., 2010; Vos et al., 2019a). There are good examples from north-western Canada (e.g., Radosavljevic et al., 2016; Irrgang et al., 2019), north-western Alaska (e.g., Farquharson et al., 2018), western Greenland (Bendixen and Kroon, 2017), Svalbard (e.g., Zagórski et al., 2015) and Laptev Sea (e.g., Günther et al., 2013). However, these studies are often characterized by either a low temporal and spatial resolution (few repeated records and few sites), short timespan or small spatial extent. At the regional scale, temporal and spatial variability in coastal change has been examined in the Canadian Mackenzie Delta (Solomon, 2005), Canadian Parry Peninsula (Tanguy et al., 2023), Alaskan Beaufort Sea coast (Jorgenson and Brown, 2005; Gibbs and Richmond, 2015), and Alaskan Chukchi Sea coast (Farquharson et al., 2018; Gibbs et al., 2019). In addition, the Arctic Coastal Dynamics network (ACD) has made significant efforts to gather pan-Arctic erosion rates by reviewing previous regional studies (Lantuit et al., 2012). In addition to these, Rolph et al. (2022) have done important pioneering work on the numerical modelling of Arctic coastal erosion.

Lately, the use of Google Earth Engine for upscaling remote sensing analyses has increased rapidly and made global-scale land cover analyses feasible (e.g., Pérez-Cutillas et al., 2023). Google Earth Engine's power has also been utilized in water detection both on the coastal zone (Vos et al., 2019a, 2019b; Li et al., 2021a, 2021b; Philipp et al., 2023) and on inland waters (e.g., Beaton et al., 2019; Li et al., 2021a, 2021b; Ismail et al., 2022; Zhu et al., 2022; Liu et al., 2022; Li et al., 2022b). For example, Pekel et al. (2016) have published a near-global (c. 55° S to 78° N) dataset of surface water extent and seasonal patterns covering two epochs, 1984–1999 and 2000–2021, in Google Earth Engine. A recent pan-Arctic coastal change study analysed Synthetic Aperture Radar (SAR) data from 2017 to 2021 for estimating short-term erosion rates (Philipp et al., 2023).

In optimal conditions, detecting water from optical multispectral satellite images, such as Landsat or Sentinel-2, is a straightforward task, since the reflectance of pure, evenly illuminated sea water is very different from the reflectance of land or ice. For example, Ismail et al. (2022) and Li et al. (2022a) reviewed the development and suitability of water extraction methods from passive satellite remote sensing data. They divided existing methods into threshold segmentation (single-band or multi-band threshold methods) and image classification methods. Threshold segmentation is solely based on the spectral characteristics of water, while image classification methods can also account for the texture and spatial characteristics (Li et al., 2022a). Images can be classified using machine learning methods like support vector machine, decision tree methods, object-based methods and deep learning (Li et al., 2022a). Each of these methods have certain advantages, challenges and limitations related to, e.g., image noise, water quality, illumination, computational cost and opportunities for being automated.

The use of multispectral indices in detecting water and land, which can be applied in shoreline mapping, are among the simplest and most applied methods (e.g., Bishop-Taylor et al., 2021; Ding et al., 2021). These indices include the normalized difference water index (NDWI; McFeeters, 1996), and the modified normalized difference water index (MNDWI; Xu, 2006). They utilize the difference between green and infrared reflectances to distinguish between water and land. NDWI compares green band to the near infrared band (e.g., Landsat 8 OLI band 5 NIR) and MNDWI to the short-wave infrared band (e.g., Landsat 8 OLI band 6 SWIR1). Some of the less frequently used water indices include the tasseled cap wetness index (TCW; Crist, 1985), the automatic water extraction index (AWEI; Feyisa et al., 2014), and WIBI (Ismail et al., 2022), that utilize information from more than two bands, and empirically determined coefficients. Water extraction methods based on spectral indices are intuitive, computationally light and deal with some of the illumination differences caused by topography, weather and season. However, they often fail to classify steep topographic or urban shadows correctly (e.g., Fisher et al., 2016; Li et al., 2021a). For example, classification errors remain in the steep north-facing coasts of the Arctic in the global surface water dataset by Pekel et al. (2016). Determining the appropriate threshold is another key aspect that influences the classification accuracy of multispectral indices. However, previous studies indicate that the true benefit of image-specific thresholds might be marginal (Feyisa et al., 2014), and they require more control and computing power than using pre-defined global thresholds.

Supervised classification methods have also been widely applied in coastal land cover studies (e.g., Vos et al., 2019a). The most popular methods include random forest (Breiman, 2001; Zhang and Yang, 2020), support vector machines (Cortes and Vapnik, 1995; Adam et al., 2014), and neural networks (Civco, 1993; Vos et al., 2019a). Supervised classification may help overcome local classification challenges related to water quality or illumination. However, production of the training data creates an obstacle for automized analyses of large volumes of satellite data and large areas (e.g., Foody and Arora, 1997). To overcome this limitation, the algorithms can be pre-trained and then applied globally (e.g., Vos et al., 2019a). In addition, data fusion can be utilized to automatically create training data even separately for each image (e.g., Li et al., 2021c; Naboureh et al., 2023).

Another challenge in shoreline detection are the short-term water level fluctuations, that have an impact on the location of the instantaneous shoreline at the acquisition time of single satellite images. This greatly influences landcover data extracted from single images, particularly in meso- and macro-tidal coasts (Ding et al., 2021; Vos et al., 2023). This phenomenon can be accounted for using tidal corrections (e.g., Vos et al., 2023), but utilizing dense image timeseries might be even more effective (Laengner et al., 2019; Ding et al., 2021).

Sea ice and ice sheets are characteristic components of the Arctic coastal zone, also during the summer season. While they have important consequences for coastal geomorphological processes, they also often constitute the shoreline. For example, the retreat of the marine-terminating glaciers of the Arctic creates new shoreline and exposes new landscapes to paraglacial and marine processes (Kavan and Strzelecki, 2023). Remote sensing of sea ice extent is a well-establish field and is mainly based on passive microwave data (Sandven et al., 2023). Optical images, such as multispectral Landsat images, are also used in sea ice analyses whenever weather and illumination conditions allow (Sandven et al., 2023). The normalized difference snow index (NDSI; Hall et al., 1995) can be used to extract snow and ice using green and short-wave infrared bands (Landsat 8 OLI band 5 SWIR1). However, as it is identical to the MNDWI and very similar to NDWI, it cannot be used for separating ice and water. Water-ice classification therefore requires more information than a single normalized difference index (e.g., Barbieux et al., 2018). Pixel-based methods like the water-resistant snow index (WSI; Sharma et al., 2016; Donmez et al., 2021), the water-ice classification index based on local texture (WICI; Barbieux et al., 2018), and $NDWI_{ns}$ and $NDSI_{nw}$ (Yan et al., 2020) have been developed to overcome this obstacle. Supervised classification also performs well in this task (e.g., Yang et al., 2022). The common feature for these methods is that they take advantage of the high infrared reflectance of ice compared to water.

Based on previous coastal change studies, we identify a need for a multitemporal, medium-resolution pan-Arctic dataset of coastal land cover spanning several decades. Such data would enable examination of geomorphological patterns and processes that operate at varying spatial and temporal scales. While satellite radar data have been proven to be applicable in calculating short-term erosion rates, optical multispectral satellite images must be considered to capture coastal change over

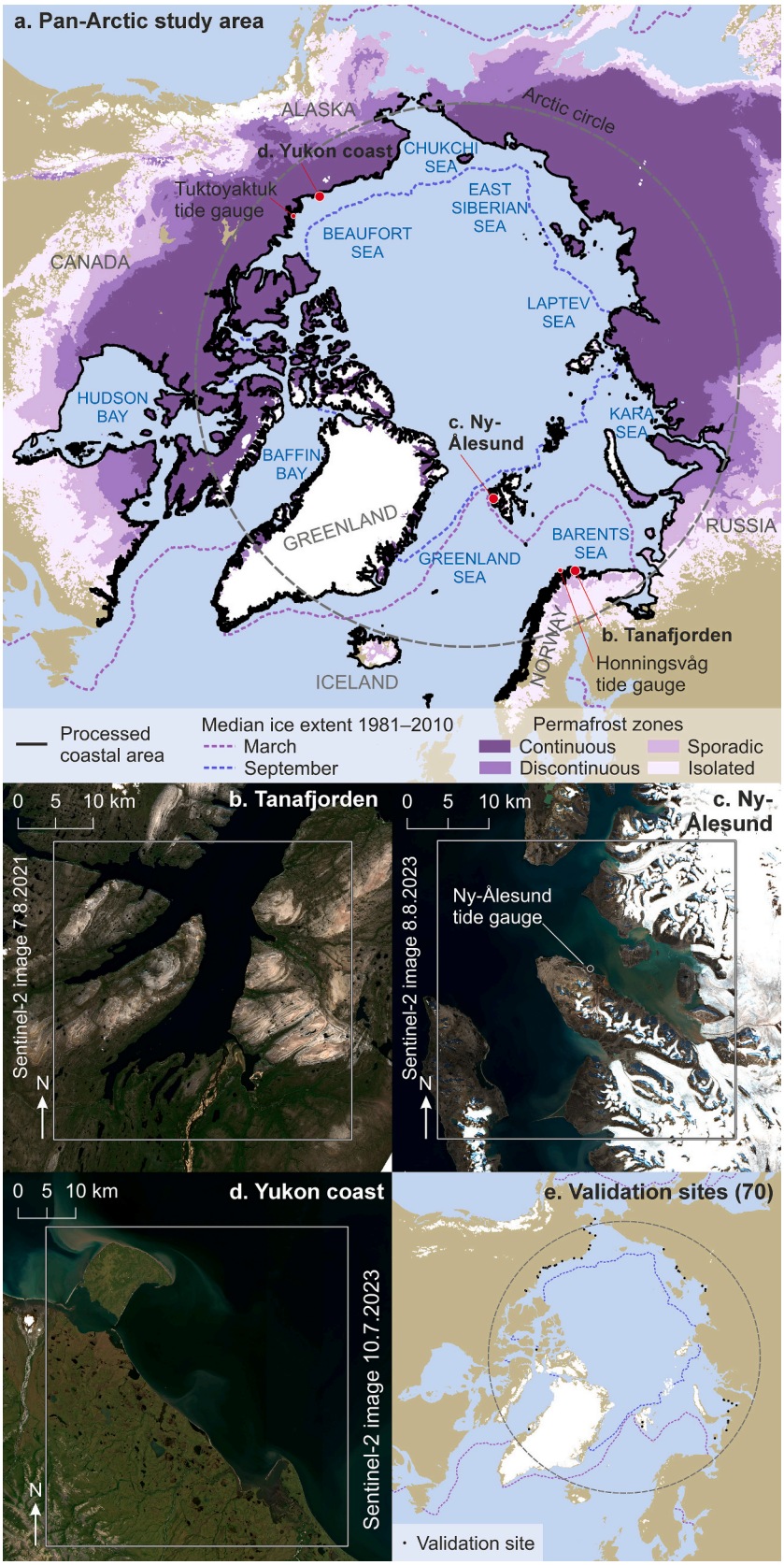

Fig. 1. The pan-Arctic study area and the three calibration sites. Panel a. shows the study area and locations of the calibration sites. Panels b.–d. present the three calibration sites: Tanafjorden (panel b.) in the Norwegian Barents Sea coast, Ny-Ålesund (panel c.) in the high-arctic Svalbard, and Yukon coast (panel d.) in the Canadian Arctic. Panel e. shows the distribution of the 61 validation sites around the Arctic coast. Spatial data: National Snow and Ice Data Center, Obu et al., 2018, and Copernicus Sentinel.

longer timespans like 40 years. In the Arctic, we believe that a coastal land cover dataset should consider land, water and summer ice as separate classes. Based on previous remote sensing research, we believe that making robust, computationally light continental-scale coastal change analyses in the Arctic is possible when utilizing Google Earth Engine's performance, a combination of multispectral indices and supervised classification, spatial data fusion, and temporal decision fusion. We hypothesize that it is possible to overcome the bottleneck of having suitable training data for supervised classification by creating the training dataset without user input from complementary spatial data. The training data can be, for example, generated from publicly available land cover and topographic datasets using spatial analyses to identify stable and representative pixels.

Thus, the aim of this study was to produce a pan-Arctic 40-year time-series of Arctic coastal change by developing a simple data fusion approach. The procedure utilized open multispectral Landsat satellite data by taking advantage of Google Earth Engine's computation power and cloud data collections. In this paper, we describe the main components and capabilities of the procedure and examine the characteristics of the resulting data. These were demonstrated in three contrasting calibration sites. In addition, we validated the resulting coastal change data by comparing erosion and accretion rates against previous studies in 61 sites around the Arctic coast. This paper introduces a pan-Arctic dataset of 40-year coastal change and a validated procedure for examining coastal change anywhere in the world.

2. Study area

This study aimed at producing coastal change data for the entire Arctic coast, including all arctic islands, Iceland, Greenland, Hudson Bay, Chukchi Sea, and northern Norway (Fig. 1a). The size of the processed four-kilometre-wide coastal zone was c. 903,000 km^2 (measured in the Arctic Polar Stereographic coordinate reference system). After preliminary analyses with different coastal zone sizes, this four-kilometre-wide zone (two kilometres to either side of the present-day shoreline) was chosen as the area of interest. It was considered wide enough to accommodate most coastal changes between 1980s and 2020s and potential errors in existing shoreline dataset used in the delineation. The zone was kept as narrow as possible to minimize computing time and data management burden.

We used three contrasting calibration sites to iteratively develop and validate the procedure. The main components of the procedure were calibrated in the Tanafjorden area, at the Barents Sea coast of Norway (Fig. 1b). This relatively stable, generally ice-free and mountainous coast site provided a suitable setting for calibrating many components of the procedure. Those components of the procedure that dealt with marine-terminating glaciers and mountainous coasts were calibrated in the Ny-Ålesund area at the Greenland Sea coast of the Svalbard archipelago (Fig. 1c). Components dealing with, for example, sea ice were calibrated in the Canadian Yukon permafrost coast (Fig. 1d). The Yukon coast calibration site also represented low-lying permafrost coasts in the development of the procedure. The size of each calibration site was c. 2500 km^2 (50 km * 50 km measured in the local UTM coordinate reference system). In each calibration site and each iteration, the results were validated against independent coastal land cover data.

The final procedure was used to process the entire Arctic coastal study area. The resulting 40-year coastal change data were then validated against independent reference studies of coastal erosion and accretion rates in 61 sites (Fig. 1e) around the Arctic.

The calibration site of Tanafjorden (also 'Deanuvuotna' or 'Tenovuono'; c. 70.5° N, 28.5° E; Fig. 1b) is located in the Fennoscandian Barents Sea coasts of northern Finnmark, Norway. The calibration site included south-western parts of the Nordkinn Peninsula (Nordkinnhalvøya), the Tana River delta, and north-western parts of the Varanger Peninsula (Varangerhalvøya). This calibration site was selected since it was very familiar to the authors and could be accessed for on-site validation of the results during the COVID pandemic. As the Tanafjorden calibration site is free of sea ice and coastal ice, the mountainous area was deemed suitable for comparing the land cover classification performance between Landsat level 1 top-of-atmosphere and level 2 bottom-of-atmosphere data and comparing the performance of alternative multispectral water indices in the Arctic illumination conditions in a heterogeneous landscape. The generally stable lithified coasts of Tanafjorden were also considered suitable for examining the impact of data availability and Landsat sensor differences on the results, as true erosion rates are negligible in the area (excluding the highly dynamic delta of the Tana River). Finally, this mesotidal coast was deemed suitable for assessing the impact of the tide on detecting the boundary between land and water. Mesotidal conditions characterize the coasts of Fennoscandia, southern and western Iceland, southern and western Greenland, and western parts of the Canadian Arctic (AVISO+ FES2014 Global Tidal Range Classification).

The Tanafjorden coast is in most parts dominated by steep cliffs, typical of fjord landscape. Where rivers enter the fjord, the topography is generally flatter and regular water level fluctuations create tidal flats and salt marshes. The largest river in the area is Tana River, the border river between Norway and Finland and one of the largest in Norway. While there are some snowbeds in the mountains – patches of snow that melt late in the summer – there is no sea ice (data by National Snow and Ice Data Center), no glaciers, and no coastal permafrost in the area (Gisnås et al., 2017), despite belonging to the classes of sporadic and isolated permafrost in circumpolar datasets (Obu et al., 2018). Rivers entering the Barents Sea and their brackish deltas have an ice cover from mid-October to mid-May. The Tanafjorden calibration site has a humid subarctic climate. The annual mean temperature in Tanafjorden is around 0.5 °C and the mean annual precipitation around 513 mm (climate data from the Rustefjelbma weather station 1991–2020; Norwegian Centre for Climate Services). The coast has a seasonal snow cover and is mainly free of snow from June to mid-October. The area is characterized by a semidiurnal lunar tide with a mean tidal range of 2.3 m during spring tide (Norwegian Hydrographic Service).

The calibration site of Ny-Ålesund is located around the town of Ny-Ålesund in Svalbard (c. 78.9° N, 11.9° E; Fig. 1c). The calibration site covers southern parts of the Mitrahalvøya peninsula, Krossfjorden, southern parts of Haakon VII Land, Kongsfjorden, and northern parts of the strait of Forlandsundet and the island of Prins Karls Forland. The glaciated coast was considered suitable for comparing the performance of alternative methods for separating sea ice and terrestrial ice from bare ground and open water, and for identifying classification challenges that are characteristic of glaciated coasts. It also provided a suitable case for testing if the procedure can identify new coastlines that emerge from under the marine-terminating glaciers. Moreover, post-glacial land uplift may cause seaward shoreline displacement in this area. We wanted to test the capability of the procedure to identifying this phenomenon. Finally, the Ny-Ålesund calibration site could be used to assess the impact of the tide on our results in the micro-tidal coasts of the Arctic, i.e., majority of the Russian Arctic, northern Alaska, and western parts of the Canadian Arctic (AVISO+ FES2014 Global Tidal Range Classification).

In the Ny-Ålesund calibration site there are nine glaciers that have in the past flowed onto the ocean forming ice shelves. The ice shelves have retreated during the past decades, and a few of them have shifted from marine-terminating to land-terminating glaciers. The retreat has created new shorelines and pristine landscapes (Kavan and Strzelecki, 2023). The ocean is generally ice-free throughout the year, but parts of the nearshore freeze in winter and spring (National Snow and Ice Data Center). There is widespread permafrost in the coast (Humlum et al., 2003). The annual mean temperature in the Ny-Ålesund weather station is −4.2 °C and the measured annual mean precipitation 469 mm (1991–2020; Norwegian Centre for Climate Services). Ny-Ålesund coast has a semidiurnal tide with a mean tidal range of 1.3 m during spring tide (Norwegian Hydrographic Service).

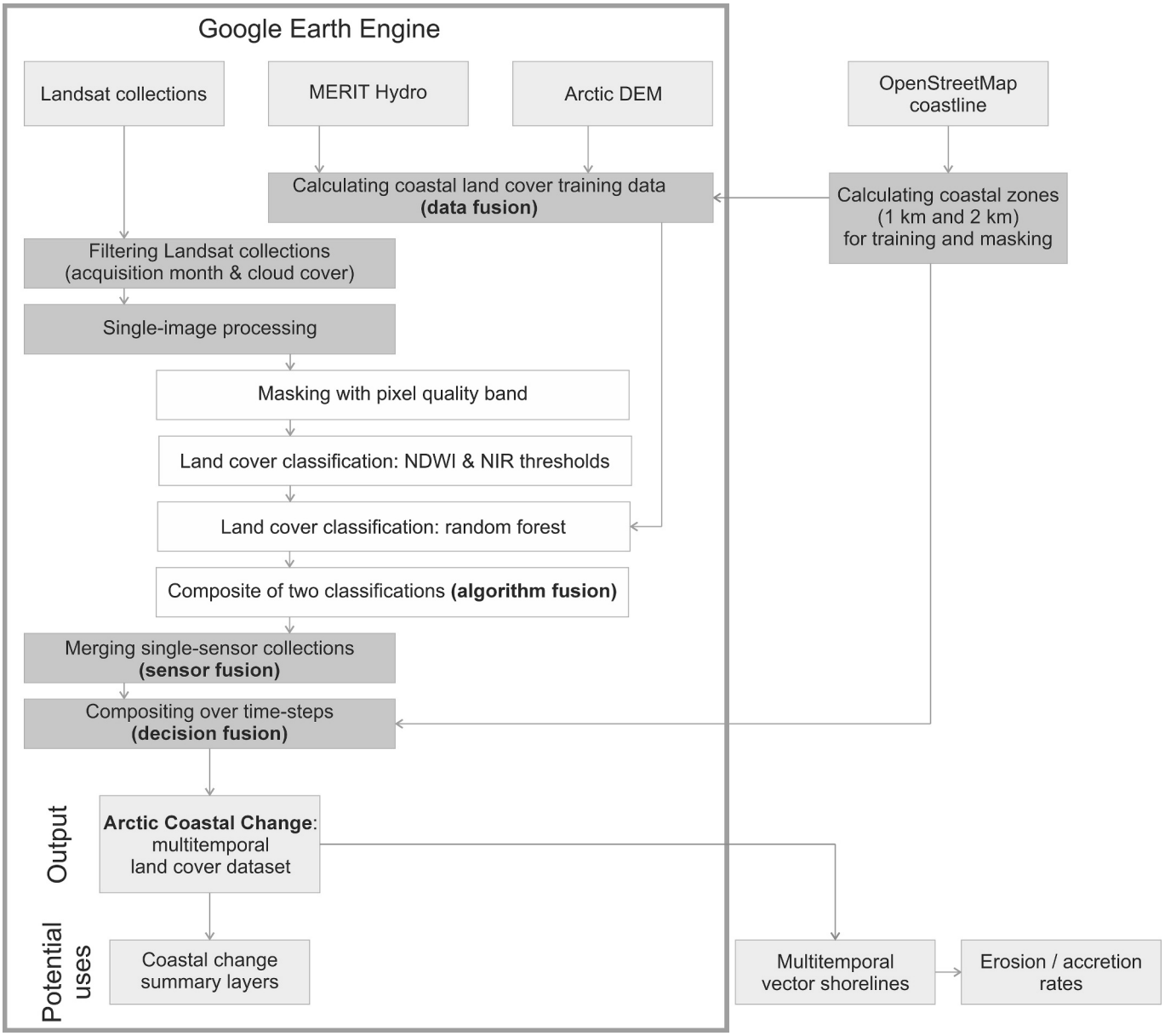

Fig. 2. Workflow of the final procedure in Google Earth Engine. The Arctic coastal zone vector data is publicly available in the Google Earth Engine for future users. The multitemporal land cover raster data can be further processed into a time-series of shorelines (vector data) for a user-defined area of interest for calculation of erosion and accretion rates.

The calibration site of Yukon coast is located in the western Canadian Arctic (c. 69.4° N, 138.7° W; Fig. 1d). It covers the Herschel Island and a section of the northeast-facing mainland coast of Yukon until the headland of Kay Point. This calibration site provided a suitable setting for validating the procedure on an unlithified, low-relief coast that is affected by permafrost thaw and shortening of the sea ice season, and for identifying potential land cover classification challenges that are characteristic of these kinds of coasts. Previous coastal erosion observations and remote sensing studies (e.g., Bartsch et al., 2020) provided opportunities to directly compare our results to previously reported erosion rates.

The Yukon coast calibration site is on the zone of continuous permafrost, and has seasonal sea ice cover, usually from October to June. The landscape is characterized by low relief, with coastal bluffs, beaches, spits, barrier islands and deltas (Irrgang et al., 2018). Erosion of the loose coastal sediments mainly occurs during the storms of the open water season in August and September (Obu et al., 2016). Based on weather data from the Komakuk Beach weather station from 1971 to 2000 (69.6° N, 140.2°W; more recent climate observations not available along the Yukon coast), the annual mean temperature was −11.0 °C and the annual mean precipitation 161.3 mm (Meteorological Service of Canada). The annual share of snowfall was 48 % of the precipitation. The mean tidal range during spring tide is c. 0.3 m (Fisheries and Oceans Canada).

3. Data and methods

3.1. Developing the procedure for processing big satellite data

The procedure development for Arctic coastal change analysis was an iterative process, aiming at testing state-of-the-art solutions and their adaptions to the diverse Arctic conditions. After each iteration, the computing performance was examined, and the outputs were validated against independent data. The iterations of the development process

aimed at building a procedure that is simple, can be applied to a range of environments across the Arctic, and computationally light enough to be scaled up to the entire Arctic coast. This was aimed at by answering mainly these questions:

- Which open multispectral satellite image collections provide useful coastal land cover information from the 1980s onward?
- Which satellite image processing level and multispectral index result in highest coastal land cover classification accuracy?
- How well can coastal snow and ice be separated from land and water using simple thresholding methods on multispectral data?
- Does decision fusion across several images result in higher classification accuracy compared to classification of one highest-quality image, and what temporal composition window optimally balances number of good observations and temporal resolution of the resulting dataset?
- Which environmental characteristics cause most notable local classification errors, and which ones can and should be dealt with in the procedure?
- How can remaining classification problems be dealt with, e.g., using data fusion and complementary open spatial data, automized supervised classification and algorithm fusion?
- Which data structure supports summarizing the coastal land cover time-series into meaningful information on Arctic coastal change?

The final automated procedure for creating coastal land cover data can be divided into nine steps (Fig. 2). The output of the procedure is a time-series dataset of coastal land cover, with three classes: land, sea, and summer ice. This multitemporal raster dataset directly allows examination of coastal erosion and accretion using change detection methods developed for raster data. It can be further processed into a time-series of shorelines (vector data) for a user-defined area of interest.

3.2. Reference data and validation

We validated the coastal land cover time-series against two types of reference data: first, the results of each iteration were validated against independent shoreline and land cover point data created for the time-period 2019–2023 for the three calibration sites: Tanafjorden, Ny-Ålesund and Yukon coast (Fig. 1a–d). Second, the final land cover results were validated by calculating erosion and accretion rates and comparing them against reference rates for 61 validation sites (Fig. 1e).

First, the validation data for the three calibration sites were created for examining the accuracy of the coastal land cover classification and the accuracy of the shoreline detection. These reference data corresponded to mean sea level conditions during c. 2019–2023. The shorelines of the calibration sites (Fig. 1a–d) were manually digitized from hand-picked remote sensing images at a 1:5000 scale. The shoreline was interpreted as the land-sea-interface when sea level is close to the long-term mean. Marine-terminating glaciers caused the shoreline to break, as we did not want to attempt estimating the location of the shoreline under ice. The four-kilometre-wide coastal zone (excluding lakes and ponds) of the calibration sites was then randomly sampled, creating 2000 reference points in each calibration site. The points were manually classified into land, sea, and summer ice (Fig. S1). In the absence of ice, points located above and below mean sea level (using previously digitized shoreline as a reference) were classified as land and water, respectively. Points were classified as ice, if they were covered by a glacier at the peak of the summer season. Sea ice was not present in any of the reference data. These reference data were created by the same coastal geomorphologist to maximize the homogeneity of the data. The interpretations were mainly based on national high-resolution orthophotos or satellite images with a pixel size of less than one metre (Tanafjorden site: “Finnmark 2018” by the Norwegian Mapping Authority; Ny-Ålesund site: “Svalbard Ortophoto GSD10 Ny-Ålesund 2008” by the Norwegian Polar Institute; Yukon coast site: Yukon high-resolution GeoEye-1 satellite imagery 2011 by the Government of Yukon), and more recent Copernicus Sentinel-2 images with a 10-m pixel size. Tidal information was used to select Sentinel-2 images that corresponded to mean sea level conditions. For the Tanafjorden calibration site (Fig. 1b), the interpretation was also based on in situ observations from October 2021.

After each iteration, error matrices comparing the modelled land cover data to the manually labelled validation points were used to calculate overall accuracy and Kappa. For the final dataset, shorelines corresponding to the time-step 2019–2023 were automatically fitted to the land cover data, and smoothed and simplified. Shoreline error distance was calculated as the distance from the manually digitized shoreline to the modelled shoreline along transects with a 30-m spacing. The analysis followed the framework of the Digital Shoreline Analysis System (DSAS) by the U.S. Geological Survey (Himmelstoss et al., 2024). The length of the analysed shorelines were 316.8 km, 199.2 km and 164.5 km for Tanafjorden, Ny-Ålesund and Yukon coast calibration sites, respectively.

Second, for validating the final multitemporal Arctic coastal change dataset against published reference data, we identified suitable scientific papers and datasets with a systematic review (see Supplementary Table S1 and Fig. S2). The review concentrated on items of the Web of Science Core Collection and the Arctic Coastal Dynamics list of peer-reviewed publications (https://arcticcoast.info/publications/27-acd-publications-list). Out of 254 screened titles and abstracts, and 77 screened full papers, we identified 40 potential studies for the review. We also identified 10 other potential papers and open datasets through the reference lists of the screened full papers (Supplementary Table S1 and Fig. S2).

From these 50 papers and open datasets, we identified 61 coastal sites (Fig. 1e) for the validation. We mainly included sites for which erosion and accretion rates had been retrieved using in situ measurements, aerial photographs, and high-resolution satellite imagery. We accepted sites whose geographical location and extent had been described in enough detail to be compared to our data, and where the temporal range of the erosion or accretion rates was specified and comparable to our results. That is, we mainly included sites for which shoreline movement rates had been reported for periods with at least nine years overlap with our study period 1984–2023. For two remote Siberian coasts we accepted rates for shorter time-periods (two and five years) to increase the spatial coverage of our validation sites. In many cases multiple papers reported erosion rates for the same sites. In these cases, we selected reference rates that had the longest temporal overlap with our study period 1984–2023, and that were reported in a way that made the comparison more exact. Studies based on satellite remote sensing that did not report validation results were not included in the comparison.

For comparing our results to reported shoreline change rates, multitemporal shorelines were automatically fitted to the land cover data for the specific validation sites. For the comparison, we examined shorelines corresponding to five-year time-steps that were as close to the reported time period of the shoreline change rate as possible. For example, the reference rate for the Drew Point site in the Alaskan Beaufort Sea coast for the time period 1979–2012 was compared to new coastal land cover data for time-steps 1999–2003 and 2009–2013, as there were not enough Landsat data for 1984–1998 in the area.

The reference erosion and accretion rates had been calculated using varying statistics, mainly as the end-point rate or the linear regression rate, and many studies did not specify the statistic. To speed up the validation process, we calculated the shoreline movement rate as the end-point rate between two shorelines in all sites.

The validation was conducted in the R software (version 4.3.3; R Foundation for Statistical Computing, 2024) with the terra (Hijmans et al., 2024) and sf (Pebesma et al., 2024) tools and in the Digital Shoreline Analysis System (DSAS) by the U.S. Geological Survey (version 6; Himmelstoss et al., 2024).

Table 1
Details of the Landsat image collections and visual, near-infrared and short-water infrared bands (VNIR / SWIR) used in the study.

Satellite and sensor	First	Last	
Landsat 5 TM	1984	2011	
Landsat 7 ETM+	1999	2024*	
Landsat 8 OLI	2013	operational in 2025	
VNIR / SWIR bands	**Landsat 5 TM / Landsat 7 ETM+**	**Landsat 8 OLI**	**Spatial resolution (m)**
Blue	1 (0.45–0.52 μm)	2 (0.45–0.51 μm)	30
Green	2 (0.52–0.60 μm)	3 (0.53–0.59 μm)	30
Red	3 (0.63–0.69 μm)	4 (0.64–0.67 μm)	30
NIR	4 (0.76–0.90 μm / 0.77–0.90 μm)	5 (0.85–0.88 μm)	30
SWIR1	5 (1.55–1.75 μm)	6 (1.57–1.65 μm)	30
SWIR2	7 (2.08–2.35 μm)	7 (2.11–2.29 μm)	30

* The quality of the Landsat 7 ETM+ images degraded after the failure of the scan line corrector in May 2003.

3.3. Landsat images

The analyses were based on the Landsat 5 Thematic Mapper (TM), Landsat 7 Enhanced Thematic Mapper Plus (ETM+) and Landsat 8 Operational Land Imager (OLI) tier 1 collections in Google Earth Engine (Table 1). Their six visible, near-infrared, and short-water infrared bands with a common spatial resolution of 30 m were considered in the procedure development (Table 1).

Other Landsat collections of the Google Earth Engine were considered unsuitable for our purpose. Namely, data catalog includes the images of Landsat 1–5 Multispectral Scanner (MSS) sensors only as raw scenes, i.e., as DN values that represent scaled, calibrated at-sensor radiance, and without pixel quality information. Thus, they were considered unsuitable for automized land cover classification. The lower spatial resolution of 60 m of the MSS images is neither directly compatible to the resolution of 30 m of the TM, ETM+ and OLI sensors onboard Landsat 4–8 satellites.

Landsat 4 TM images from 1982 to 1993 would have been suitable for complementing the satellite dataset, but the number of images was so small and the spatial coverage so heterogeneous (supplementary Fig. S3), that they were not included in the analyses. Namely, there were in practice no images from Greenland, the Arctic Canada, eastern Siberia or arctic islands (supplementary Fig. S3). The only Arctic coasts with more than ten Landsat 4 images were in the northern Alaska and western mainland Russia (supplementary Fig. S3).

The Landsat 9 satellite was launched at the beginning of this study in September 2021. Due to the short time span of Landsat 9 data, and since data availability for 2022–2023 from Landsat 7–8 was considered sufficient for the study, Landsat 9 images were not used. However, future studies on the 2020s coastal land cover change should utilize Landsat 9 OLI-2 data, particularly after the end of the Landsat 7 mission in 2024. We aimed at building a method that can later directly incorporate Landsat 9 OLI-2 data.

For this paper, we manually checked the possibility to include the lower-quality tier 2 Landsat 5 and Landsat 7 images to increase the number of observations but found that their quality was not sufficient. Namely, their large geometrical errors (radial root mean square error exceeding 12 m) led to horizontal inaccuracies that had negative impacts on the land cover classification accuracy.

We concentrated this procedure on the Arctic open water season following previous studies (e.g., Philipp et al., 2023). Namely, we processed Landsat images acquired between June 1st and September 30th (c.f., Philipp et al., 2023). With this seasonal window we aimed at avoiding as many images with coastal sea ice as possible while still including as many images as possible in the analysis. The illumination of images acquired later in the autumn were considered inadequate for coastal land cover classification. The appropriateness of the seasonal window was examined by browsing through decade-long Landsat time-series for the three very different calibration sites. We concluded that, generally, the seasonal window was useful for filtering out low-quality images and did not unnecessarily leave out many useful images. While studies focusing on certain areas would benefit from having tailored seasonal windows as the ice season and illumination conditions vary greatly throughout the Arctic, a fixed seasonal window was considered necessary for our automized procedure.

We utilized images with a cloud percentage of less than 50 %. This threshold was selected to maximize the number of observations on individual pixels, but to exclude images with a substantial proportion of noisy pixels. Even though most clouds and cloud shadows were later masked from the images, with increasing cloud percentage, also the number of undetected cloud pixels increased, thus leading to increasing number of falsely classified pixels.

We also ensured that there were enough valid pixels for supervised classification in each image, and images that did not meet this criterium were further filtered out from the image collections. First, noisy pixels were masked using the Landsat pixel quality band (generated by U.S. Geological Survey with the CFMask algorithm) and reflectance values. This step masked individual pixels that had been flagged as clouds, cloud shadows, fill pixels and image edge noise. After that, the number of valid (not masked) pixels that overlapped the land and water pixels in the training data layer were calculated for each image. Images, that had less than c. 10 km^2 of overlap with either land or water training pixels were excluded from the analyses.

3.4. Complementary spatial data

We acquired complementary spatial data to focus the processing to the Arctic coastal zone and to automatically create training data for supervised land cover classification and algorithm fusion.

For focusing the analysis to the Arctic coastal zone, we first compared available coastline products. We selected the OpenStreetMap coastline product (FOSSGIS e.V., 2023; also used by Philipp et al., 2023) for the purpose, as it is open vector data, has a global coverage and was found to be acceptably accurate in most parts of the study area. We delineated the four-kilometre-wide “coastal zone” with a two-kilometre buffer of the OpenStreetMap coastline. The resulting polygon was cropped to the study area extent, and strongly simplified to speed up the processing and rendering of the layer. It was used as the area of interest in filtering the satellite data and for visualizing and exporting the results.

For automatic training data production, we also created a narrower coastal zone polygon with a radius of one kilometre. Both coastal zone layers were published as assets in Google Earth Engine. Training data were calculated from the narrower coastal zone and existing elevation and land cover data. The MERIT Hydro permanent water dataset (Yamazaki et al., 2019) and the ArcticDEM, a two-meter digital elevation model of the Arctic (Porter et al., 2018), were selected for the purpose based on tests in the three calibration sites. Both datasets have full coverage of the Arctic study area and are hosted in Google Earth Engine.

3.5. Sea level data

To assess the impact of the tide and long-term sea level change on the position of the shoreline, we examined sea level data from tide gauges close to the three calibration sites. For the two Norwegian calibration sites, we used data by the Norwegian Hydrographic Service, accessed

Table 2
Examined multispectral water indices.

Multispectral index	Equation	Reference
Normalized Difference Water Index	NDWI = (Green − NIR) / (Green + NIR)	McFeeters, 1996
Modified Normalized Difference Water Index	MNDWI1 = (Green − SWIR1) / (Green + SWIR1) MNDWI2 = (Green − SWIR2) / (Green + SWIR2)	Xu, 2006
Automated Water Extraction Index	AWEIsh = Blue + 2.5 × Green −1.5 × (NIR + SWIR1) − 0.25 × SWIR2	Feyisa et al., 2014
WIBI	NDWI – NDBI, where: NDBI = (SWIR1 – NIR) / (SWIR1 + NIR)	Ismail et al., 2022

through the API for water level data (https://api.sehavniva.no/tideapi_en.html). From the Honningsvåg tide gauge, c. 100 km from the Tanafjorden calibration site (Fig. 1a), sea level data were available for 1988–2023. Data from the Ny-Ålesund tide gauge (Fig. 1c) was available for 1992–2023. For the Yukon coast calibration site, we used data by the Fisheries and Oceans Canada, accessed through the Canadian Tides and Water Levels Data Archive (https://www.isdm-gdsi.gc.ca/isdm-gdsi/twl-mne/index-eng.htm). Water level data from the Tuktoyaktuk tide gauge (station 6485), located c. 220 km to the east (Fig. 1d) from the Yukon coast calibration site, was available for 2003 onwards, and for 1960s and 1970s.

For all calibration sites, we examined long-term sea level trends for 1970–2023 to see how they are reflected in the position of the shoreline. As our procedure aimed to deal with short-term coastal changes, mainly caused by tidal sea level fluctuations, we examined how the Landsat acquisition time sea levels correspond to mean sea level and tidal impacts (cf. Philipp et al., 2023).

3.6. Multispectral water indices

We examined the performance of five multispectral water indices (Table 2) in separating land and water pixels. We considered the version of the Automated Water Extraction Index that was specifically design for areas with deep shadows (AWEIsh; Feyisa et al., 2014). The comparison was done in two calibration sites, Tanafjorden and the Yukon coast, that had little terrestrial ice during the summer months, and for years 2019–2023. The Tanafjorden calibration site was also suitable for examining the performance in areas with deep shadows. First, we classified all cloud-masked images based on the five water indices and a fixed threshold of 0 (negative values = land, positive values = water). Second, we calculated the mode class for each pixel for 2019–2023. This temporal composition strategy reflects the final procedure described in the paper. We compared the classification performance in the two calibration sites both visually and against the c. 2000 validation points (excluding points classified as ice). To ensure that the results apply to the 1980s–2010s and to Landsat 5 data, the analysis was repeated in the two calibration sites for years 1984–1988 (results reported in the Supplement).

3.7. Comparison of temporal decision fusion and best images

We applied temporal decision fusion following Laengner et al. (2019). In temporal decision fusion, a dense time-series is summarized to extract more robust and accurate information for a specific period than from an individual observation. In the context of coastal land cover classification, it is based on the idea that if the number of observations on each pixel is high enough, we can assume that most water-level, weather, illumination, and ice and snow conditions have been observed (c.f. Laengner et al., 2019). Accordingly, it can be assumed that if a large number of individual images is summarized by, e.g., calculating the median land cover class for each pixel, it will give a reliable estimate of average land cover distribution. Temporal decision fusion also effectively removes noise caused by, e.g., clouds or cloud shadows, producing more accurate results than those from single images (Laengner et al., 2019).

First, we examined in the Tanafjorden calibration site if a single highest-quality image or a temporal composite image provides more accurate results on long-term coastal land cover distribution. The analysis was done for the last five-year period 2019–2023, and then repeated for the first time period 1984–1988.

The highest-quality image was selected by first identifying all available Landsat images for the time period and calibration site that were acquired in July or August, i.e., during the two months with least ice cover and highest light availability. We then masked low-quality pixels using pixel quality data and calculated the number of valid pixels within the calibration site. The image with largest number of valid pixels was selected as the highest-quality image. No sea level data was used in selecting the image, as such data are not available through Google Earth Engine, and the purpose was to build a fully automized procedure. However, the sea level of the highest-quality image was later determined for this paper from the Norwegian Hydrographic Service.

The composite land cover layer was calculated by first identifying all suitable images acquired between June and September, then filtering them to images with cloud cover less than 50 %, masking low-quality pixels, and applying the land-water-ice classification separately for each image. We then calculated the post-classification composite land cover class layer from all images acquired during the five-year time period, hereafter referred to as time-step. The composite land cover for each pixel was calculated as the mode of single-image values. For each five-year time-step, pixels with less than five valid observations were deemed unreliable and masked. This composite land cover layer was then compared to the single-image land cover layer.

Finally, we examined how the length of the time-step influenced the averaging performance of the temporal decision fusion and the data availability. This was done by calculating the missing data (pixels with <5 observations) fraction for the entire 40-year time-period for time-steps of varying length (1 to 10 years).

3.8. Automized supervised classification and data fusion

We examined the possibility to apply one commonly used supervised classification algorithm, random forest, to improve classification accuracy in areas that were difficult to classify using simple global rules, such as NDWI and NIR thresholds. Due to the large size of the classification task, the supervised classification needed training data that was already hosted in Google Earth Engine and that could be processed into a suitable format automatically. As our analyses indicated that ice and snow can be reliably detected without supervised classification, and that it was difficult to produce image-specific training data on the ice class, the areas originally classified as ice where masked from the random forest classification.

Our goal was to, without human input, identify pixels from each satellite image, that have always been land or sea for the past 40 years. As the coast is expected to be dynamic in some areas, pixels located close to the modern-day shoreline were not used for training. Results from previous iterations indicated that land areas with deep mountain shadows were most difficult to classify correctly. Thus, we created a three-class training dataset: water, land, and mountain shadows. After initial classification, the mountain shadow class was merged to the land class.

First, all non-ice pixels were classified either as land or as water based on the MERIT Hydro permanent water dataset (Yamazaki et al., 2019). Second, land and water pixels closer than 1000 m to the OpenStreetMap coastline were masked out from the training data. Third, mountain shadows were calculated separately for each image from the ArcticDEM (Porter et al., 2018). The elevation model was first cleaned up from outliers located in the sea, by using the MERIT Hydro dataset.

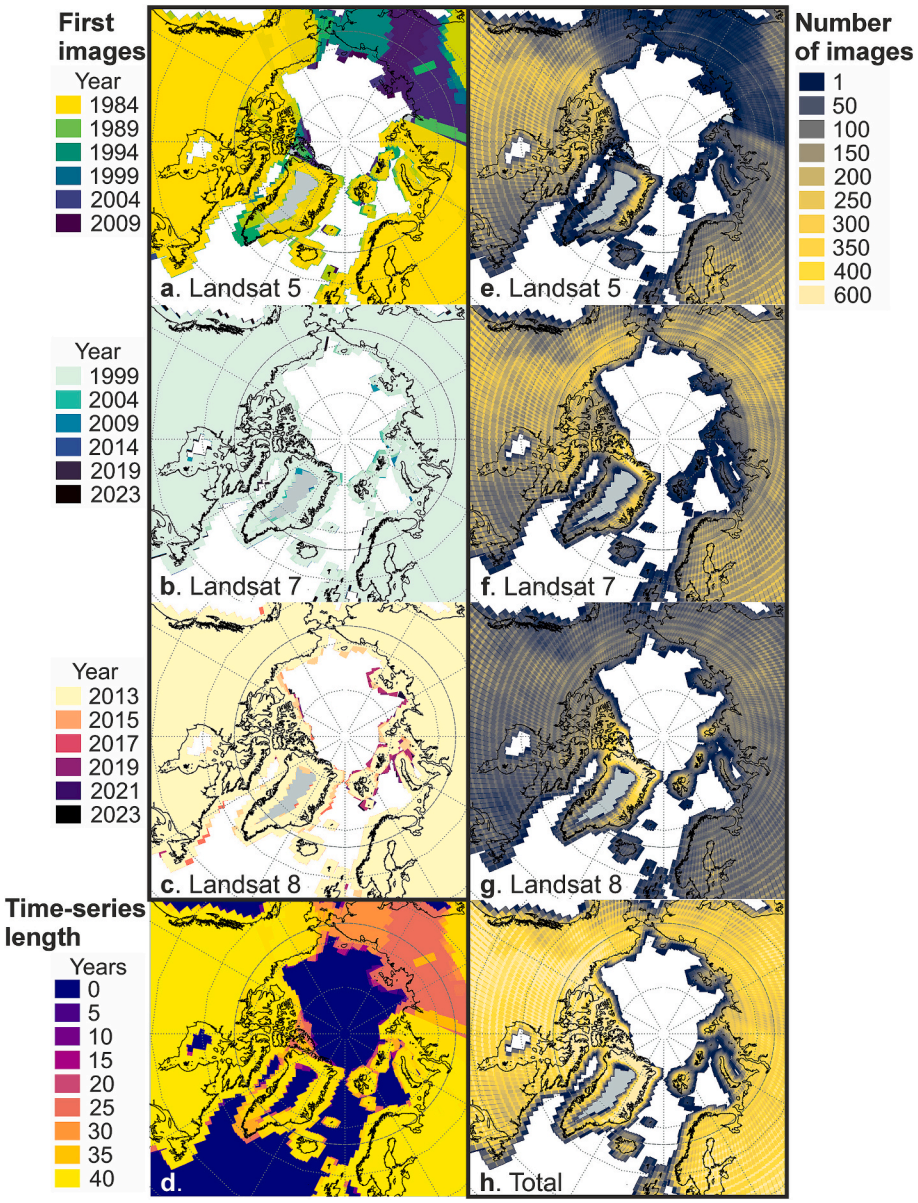

Fig. 3. Landsat data availability in the Arctic. Panels a., b. and c. show the year of the first Landsat 5, Landsat 7, and Landsat 8 image held in Google Earth Engine, respectively. Panels e., f. and g. show the number of potential Landsat 5, Landsat 7, and Landsat 8 images, respectively. Panel d. shows the length of the Landsat time-series, and panel h. the total number of all Landsat images. The potential images were those acquired from June to September and with cloud cover less than 50 %.

Table 3
Accuracy of the land-water classification based on NDWI separately for the three Landsat sensors on independent validation point data in the Tanafjorden calibration site in 2019–2023 and 1984–1988.

Sensor	Landsat 7 ETM+	Landsat 8 OLI	Landsat 5 TM
Time-step	2019–2023	2019–2023	1984–1988*
Overall accuracy	98.30	98.90	97.95
Kappa	0.965	0.977	0.957

*Note that the validation point data represents the time-period 2019–2023. Therefore, not all differences between the validation data and the predicted land cover in 1999–2002 are classification errors but some are changes in the distribution of land and water.

The mountain shadows were calculated with the ee.Terrain.hillShadow function, using image-specific sun aspect and zenith information. Since most of the problematic mountain shadows are both located close to the shoreline and are relatively stable, none of the mountain shadow pixels were masked out from the training data layer. Finally, the land/water and mountain shadow layers were combined into one three-class training data layer.

Training points were randomly picked from the training data layer separately for each satellite image. A stratified random sampling strategy (ee.Image.stratifiedSample function) was used to extract 500 points from each class within the image footprint and the four-kilometre-wide coastal zone. The random forest classifier was trained using information from the NIR band and the NDWI layer only. This selection was done after first including all Landsat bands and the NDWI layer and examining variable importance in the random forest classifier and choosing the ones with highest impact on the classification. The number of bands was reduced to minimum to minimize computing cost.

We looked for an efficient way to combine coastal land cover information from the simple and random forest classifications in a way that leveraged the best aspects of both. Namely, NDWI provided superior results in sunlit and shallow areas, while the supervised classification was more accurate in mountain shadows. We tested and validated

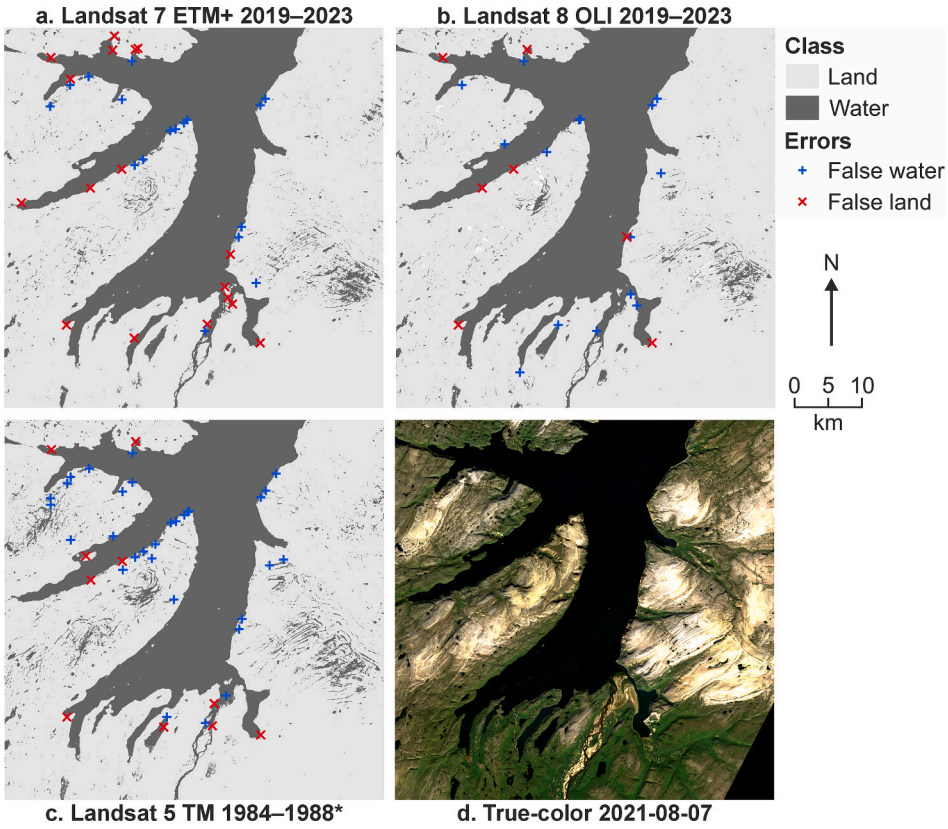

Fig. 4. Simple land-water classification for three Landsat sensors. Visualization of the land-water classification based on NDWI separately for the three Landsat sensors in the Tanafjorden calibration site: Landsat 7 ETM+ (a) and Landsat 8 OLI (b) in 2019–2023, and Landsat 5 TM (c) in 1984–1988. The figure also presents the validation points that were falsely detected as water or land (false water = land detected as water; false land = water detected as land). A Sentinel-2 true-colour image (d) is shown as reference. *Note that the validation point data represents the time-period 2019–2023. Therefore, not all differences between the validation data and the predicted land cover in 1984–1988 (c) are classification errors but some are changes in the distribution of land and water.

Table 4
Accuracy of the top-of-atmosphere and bottom-of-atmosphere classifications. The table reports the accuracy of the NDWI-based classifications for level 1 top-of-atmosphere (TOA) and level 2 bottom-of-atmosphere (BOA) Landsat imagery on independent validation point data. Panel a. shows the results for the Tanafjorden calibration site and panel b. for the Yukon coast site in 2019–2023. The highest overall accuracy for each calibration site and time-period is highlighted with bold text.

a. Tanafjorden 2019–2023		
Landsat product	TOA	BOA
Overall accuracy	96.35	**98.75**
Kappa	0.925	0.974
b. Yukon coast 2019–2023		
Landsat product	TOA	BOA
Overall accuracy	97.90	**99.05**
Kappa	0.958	0.981

different options during the process and reported in this paper the results of the chosen method. The method that resulted in highest classification accuracy in the three calibration sites while keeping the computing time tolerable divided each image into sunlit pixels and pixels with mountain shadows. For the sunlit area, the final land cover class was determined based on the original class layer and for mountain shadow pixels the class was determined from the random forest class layer. As this was done separately for each image using image-specific information on sun angles, the temporally varying impact of topography on surface reflectance was accounted for.

4. Results

4.1. Procedure development

4.1.1. Data availability

The Landsat 5, Landsat 7 and Landsat 8 image collections held in Google Earth Engine include images from 1984, 1999, and 2013 onward, respectively. None of these image collections cover the central parts or the northernmost tip of Greenland (north of c. 82.5° N; Fig. 3). The northernmost coast of the Canadian Ellesmere Island (north of c. 82.5° N; Fig. 3) is not covered by Landsat 5 or Landsat 7 images (Fig. 3). The Landsat 5 collection has data gaps also elsewhere in the Ellesmere Island, along the east coast of the southernmost Greenland, and in the eastern Taimyr Peninsula in Russia (Fig. 3).

Although large parts of the Arctic coast were observed by Landsat 5 already during 1984–1988, first images of the southern Greenland and westernmost Alaska date back to early 1990s (Fig. 3). The first Landsat images of the easternmost Siberia are from 1995, but no Landsat 5 images were acquired along the coasts of the Laptev Sea, the East Siberian Sea, the New Siberian Islands and Wrangel Island, until 2005–2007 (Fig. 3). In these areas, as well as in the eastern Taimyr Peninsula, northernmost Ellesmere Island and Greenland, and south-eastern Greenland, the first images were taken by Landsat 7 in 1999 or 2000 (Fig. 3).

The total length of the Landsat time-series reflects the acquisition year of the first Landsat 5 image and is generally at least 24 years along the Arctic coast (2000–2023; Fig. 3). The length of the time-series is 35–40 years along all coasts of the European Arctic, along the Canadian coast until c. 80° N, along the Alaskan coast until c. 165° W, in the central Greenland, and in the western Russian Arctic until c. 100° E

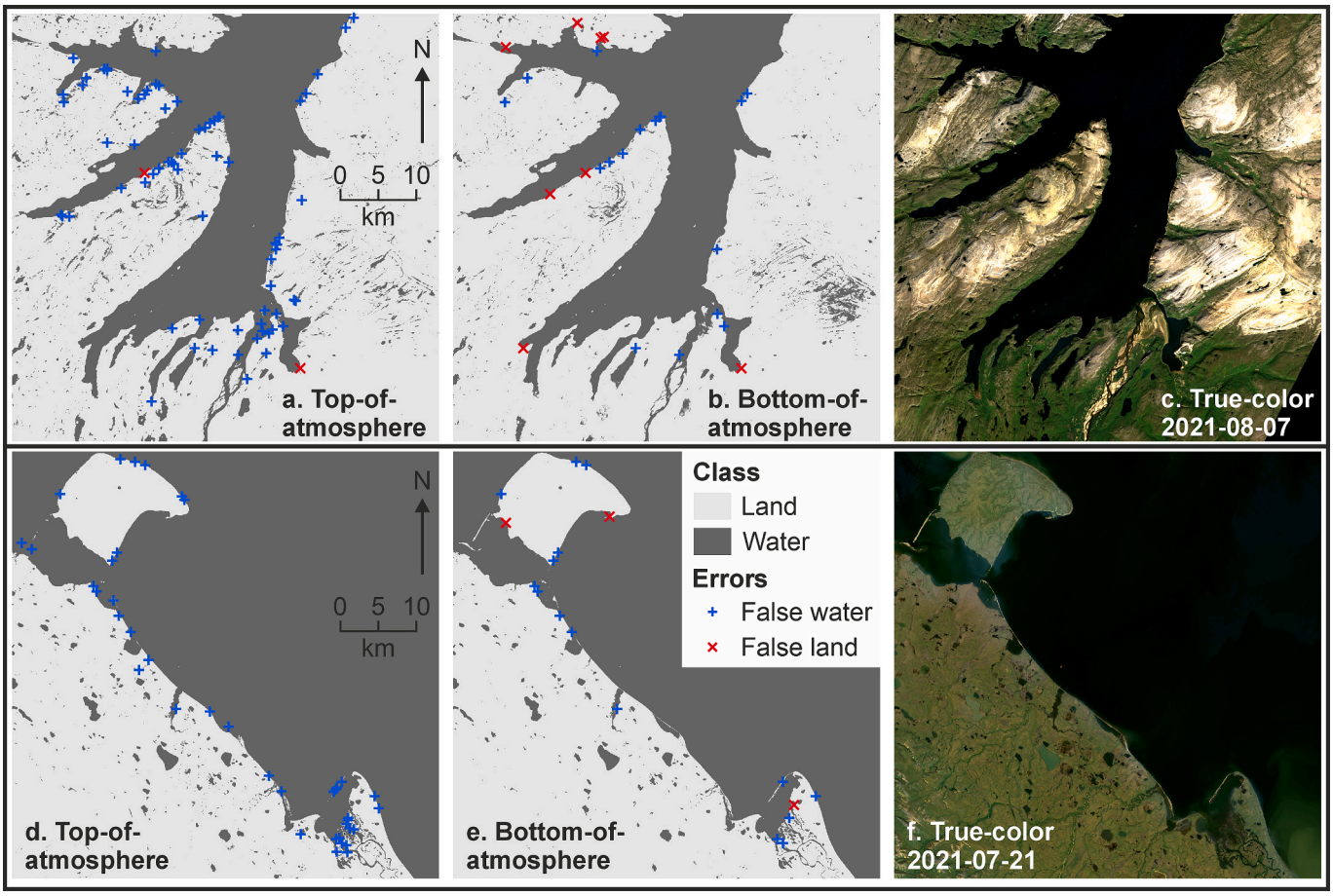

Fig. 5. Comparison of land-water classifications between Landsat top-of-atmosphere and bottom-of-atmosphere imagery. Panels a.–b. compare the classifications in the Tanafjorden calibration site and d.–e. in the Yukon coast site. Both classifications are based on NDWI and results are shown for the time-period 2019–2023. The figure also presents the validation points that were falsely detected as water or land (false water = land detected as water; false land = water detected as land). Landsat 8 OLI true-colour images are shown as reference in panels c. and f.

Table 5
Accuracy of classifications based on alternative multispectral indices. The table presents accuracies of land-water classifications based on five alternative multispectral water indices determined against independent validation point data. Panel a. shows the accuracy in the Tanafjorden calibration site and panel b. in the Yukon coast site in 2019–2023. The highest overall accuracy for each calibration site is highlighted with bold text.

a. Tanafjorden 2019–2023					
Multispectral index	NDWI	MNDWI1	MNDWI2	AWEIsh	WIBI
Overall accuracy	**98.75**	98	96.05	96.4	98
Kappa	0.974	0.959	0.919	0.926	0.959
b. Yukon coast 2019–2023					
Multispectral index	NDWI	MNDWI1	MNDWI2	AWEIsh	WIBI
Overall accuracy	**99.05**	98.9	97.9	98.32	98.9
Kappa	0.981	0.978	0.958	0.966	0.978

(Fig. 3).

4.1.2. Landsat sensor performance

We confirmed that all three selected Landsat sensors, namely Landsat 5 TM, Landsat 7 ETM+, and Landsat 8 OLI, can be used for coastal land cover classification with similar performance, with overall accuracy of more than 97 (Table 3). Two factors were expected to decrease the performance statistics. First, the performance of the Landsat 5 TM sensor was examined by comparing modelled land cover in 1984–1988 against observed land cover in 2019–2023. Second, the performance of the Landsat 7 ETM+ data was examined in 2019–2023, i.e., after the scan line corrector failure. Despite these factors, the classification performance of the Landsat 5 TM and Landsat 7 ETM+ sensors was only slightly lower than that of Landsat 8 OLI (Table 3).

With all sensors, the classification errors were focused on the shoreline (Fig. 4). Most of them were likely caused by mixed pixels, i.e., pixels at the border of land and water, whose reflectance values are influenced by both land cover classes. The classification errors were also concentrated in other similar areas with all sensors, particularly on steep north-facing shores (Fig. 4), where deep mountain shadows complicate the classification. Namely, the surface reflectance of land areas in deep mountain shadows is so low across all spectral bands that they are difficult to separate from water even using multispectral indices. The land cover classification based on Landsat 7 data had more false land pixels than that based on Landsat 8, potentially because of the inferior Landsat 7 data quality after the failure of the scan line corrector in May 2003, or lower radiometric resolution (Fig. 4a–b). The land cover classification based on Landsat 5 (Fig. 4c) had more false water pixels than the other two. Many of these were not located at the shoreline, but on the north-facing mountain slopes (Fig. 4c), thus not impacting shoreline displacement information gained from the data. Many of these false classifications may have been caused by deep mountain shadows, that may make classification of Landsat 5 images, with lower radiometric resolution, more challenging than classifying Landsat 8 images.

4.1.3. Landsat processing level

Based on comparison of land cover classifications with Landsat data of different processing levels in the Tanafjorden and Yukon coast

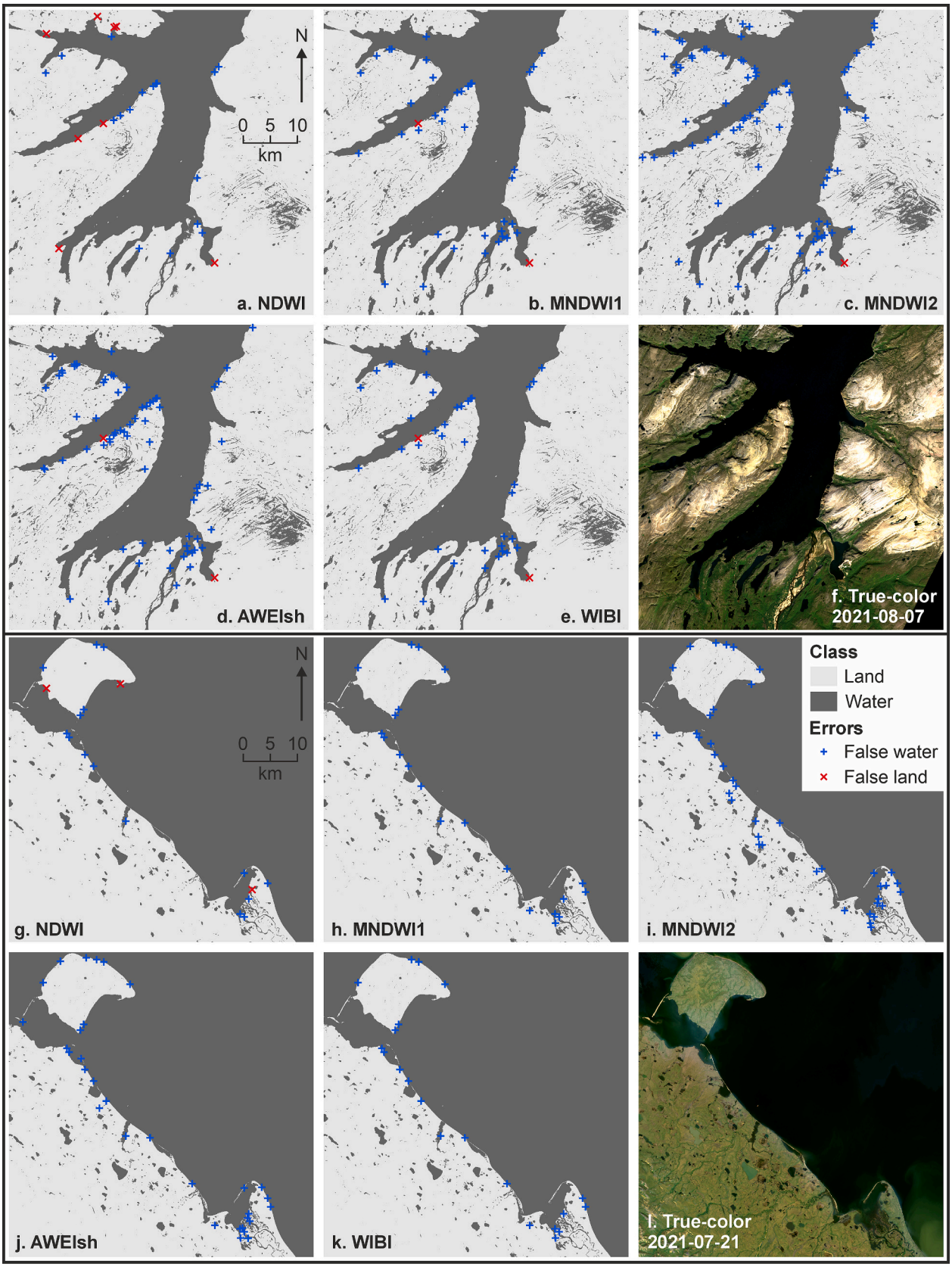

Fig. 6. Comparison of land-water classifications based on five alternative water indices. Panels a.–e. show results in the Tanafjorden calibration site and panels g.–k. in the Yukon coast site for the time-period 2019–2023. The figure also presents the validation points that were falsely detected as water or land (false water = land detected as water; false land = water detected as land). Landsat 8 OLI true-colour images (panels f. and l.) are shown as reference.

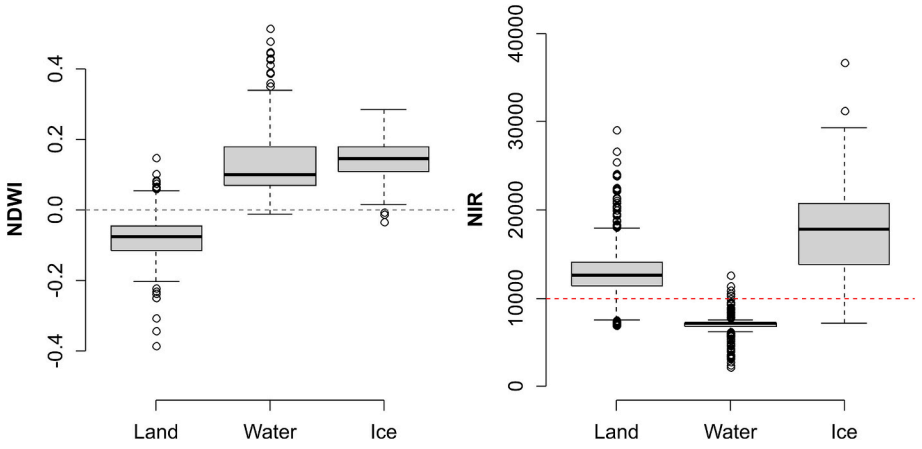

Fig. 7. Reflectance of three coastal land cover types. The figure shows boxplots of NDWI and NIR reflectance in a median composite of 2019–2023 summer (June–September) Landsat 8 OLI images for a sample of coastal land (818), water (1056) and ice (126) points in the glaciated Ny-Ålesund calibration site.

Table 6
Confusion matrices for threshold-based land-water-ice detection. The table compares 2000 manually labelled reference points to the land cover classification based on Landsat 8 OLI in 2019–2023 in the glaciated Ny-Ålesund calibration site. See Fig. 8b for the location of the misclassified points.

	Predicted		
Label	Land	Water	Ice
Land	782	32	4
Water	0	1052	4
Ice	6	10	110

calibration sites for the period 2019–2023, level 2 bottom-of-atmosphere data uniformly resulted in better results than top-of-atmosphere data (Table 4). The results for the period 1984–1988 supported the selection of the bottom-of-atmosphere images (Supplementary Table S2). Thus, all consequent iterations and the final procedure processed Landsat level 2 data with pixel values ranging from 1 to 65,455. In the Earth Engine Data Catalog, these collections were "USGS Landsat 5 Level 2, Collection 2, Tier 1", "USGS Landsat 7 Level 2, Collection 2, Tier 1", and "USGS Landsat 8 Level 2, Collection 2, Tier 1".

With the bottom-of-atmosphere data, the only classification errors were encountered at the shoreline and were likely caused by mixed pixels (Fig. 5). Classifications based on top-of-atmosphere data resulted in a higher number of false water detections, particularly in steep north-facing shores and in very shallow areas (Fig. 5).

4.1.4. *Comparison of multispectral water indices*

Based on our comparison in the Tanafjorden and Yukon coast calibration sites in 2019–2023, NDWI outperformed all other multispectral water indices (Table 5). Namely, validation against the independent point sample indicated that a land-water classification based on NDWI resulted in the highest overall accuracy and highest Kappa in both calibration sites (Table 5). The results for the period 1984–1988 supported the selection of NDWI as the basis for the classification (Supplementary Table S3).

Visual inspection of the results on map showed that the outputs from classifications based on five water indices were similar, but NDWI

Table 7
Accuracy and missing data fraction of single-image and temporal composite classifications. The table reports accuracy statistics and the fraction of missing value pixels for land-water-ice classifications for a single highest-quality Landsat image ("best") and the post-classification mode composite in the Tanafjorden calibration site in 2019–2023. The highest overall accuracy for each time-period is highlighted with bold text.

	Best	Composite
Overall accuracy	98.6	**98.9**
Kappa	0.97	0.98
NA pixels (%)	9.0	< 0.1

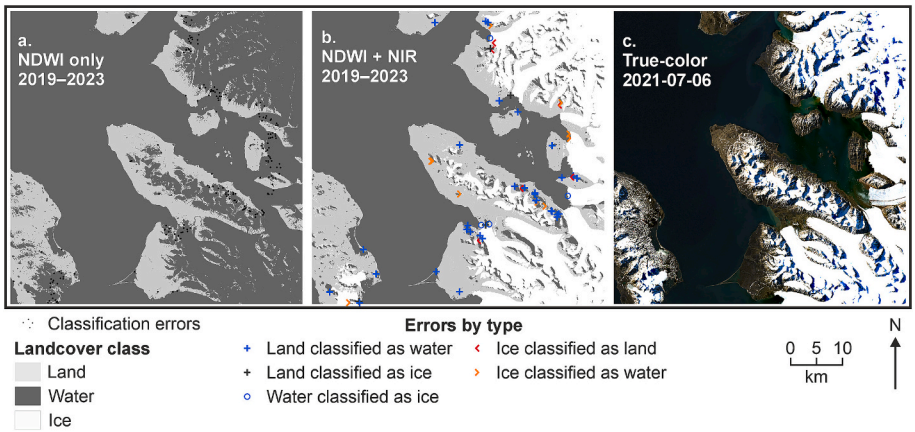

Fig. 8. Improvement of classification accuracy with introduction of an ice threshold. Panel a. shows the land-water classification based on NDWI only and panel b. the land-water-ice classification based on NDWI and NIR reflectance in the glaciated Ny-Ålesund calibration site during 2019–2023. Remaining classification errors, compared to the reference data, are shown in panel b. A representative Landsat true-colour image is shown for reference in panel c.

Table 8
Distribution of the number of observations. The table reports the distribution (% of all pixels) of per-pixel number of valid satellite observations for each calibration site and five-year time-step. Observation count range with highest number of pixels for each time-step is highlighted with bold text.

Observations	1984–1988	1989–1993	1994–1998	1999–2003	2004–2008	2009–2013	2014–2018	2019–2023
Tanafjorden								
0–4	0.1	0.6	10.9	0.9	0.1	0.4	0.1	< 0.1
5–9	2.9	17.5	**62.4**	6.3	2.3	2.4	1.0	< 0.1
10–14	14.4	**42.8**	23.4	26.5	6.8	5.7	2.7	0.7
15–29	**79.5**	39.0	3.4	**66.3**	**79.7**	**67.5**	42.9	15.8
30–	3.1	–	–	–	11.1	23.9	**53.3**	**83.4**
Ny-Ålesund								
0–4	**100.0**	0.6	**78.2**	2.6	31.8	< 0.1	–	–
5–9	–	**57.4**	21.8	**84.8**	**68.2**	11.9	–	–
10–14	–	42.0	–	12.5	< 0.1	**62.6**	< 0.1	< 0.1
15–29	–	< 0.1	–	< 0.1	–	25.5	2.9	< 0.1
30–	–	–	–	–	–	–	**97.1**	**100.0**
Yukon coast								
0–4	< 0.1	< 0.1	< 0.1	–	–	–	–	–
5–9	18.0	< 0.1	< 0.1	< 0.1	–	–	–	–
10–14	**44.4**	0.1	0.2	< 0.1	–	< 0.1	–	< 0.1
15–29	37.6	40.2	**96.4**	46.8	0.1	0.1	< 0.1	0.1
30–	–	**59.7**	3.4	**53.2**	**99.9**	**99.9**	**100.0**	**99.9**

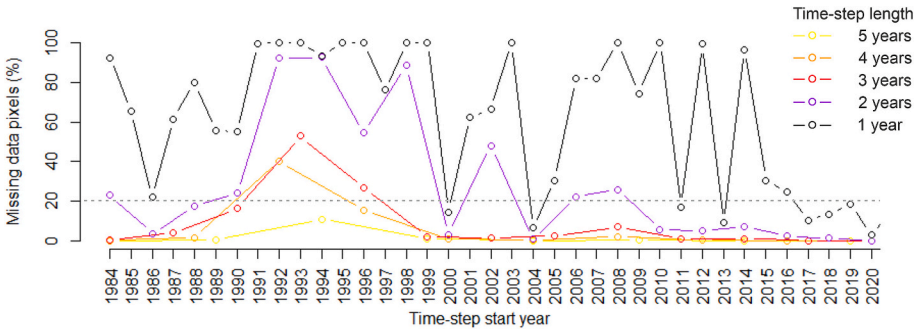

Fig. 9. Fraction of missing data pixels in the time-step composites in the Tanafjorden calibration site, with different time-step lengths. In the land cover time-step composite, a pixel with less than five observations is considered missing data.

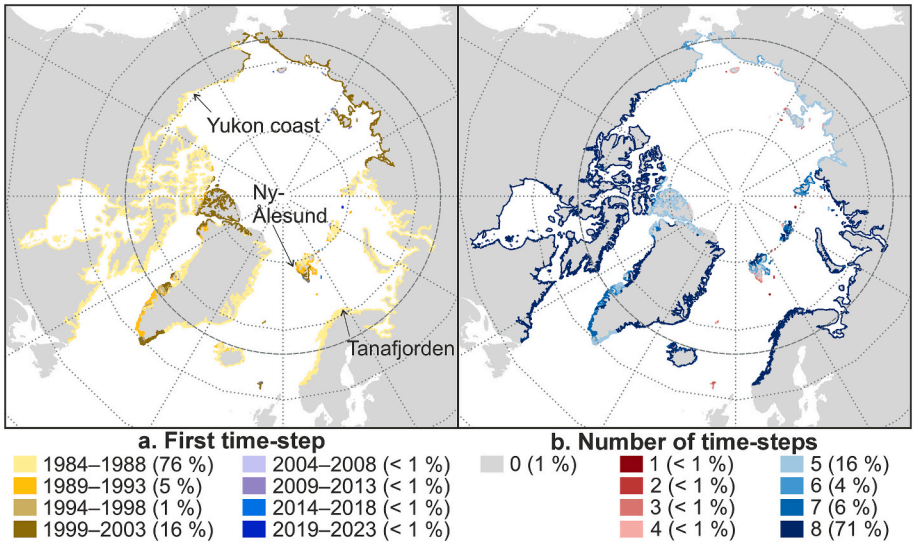

Fig. 10. Distribution of availability of Landsat imagery for time-step composites. Panel a. shows the distribution of the first time-step with a valid land cover observation in the time-series, and panel b. the number of time-steps. Corresponding fractions of the Arctic coastline are reported in the figure keys.

resulted in classifications with least errors at the coastline (Fig. 6). Notably, compared to NDWI, the false detections of water were larger both in the coastal zone and further inland with all other water indices (Fig. 6).

4.1.5. *Extraction of summer ice*

Based on literature, we developed a simple method that uses the difference in near-infrared reflectance between water and ice to group pixels with high NDWI values into the two classes. Based on a sample of pixel values for manually labelled points in the glaciated Ny-Ålesund

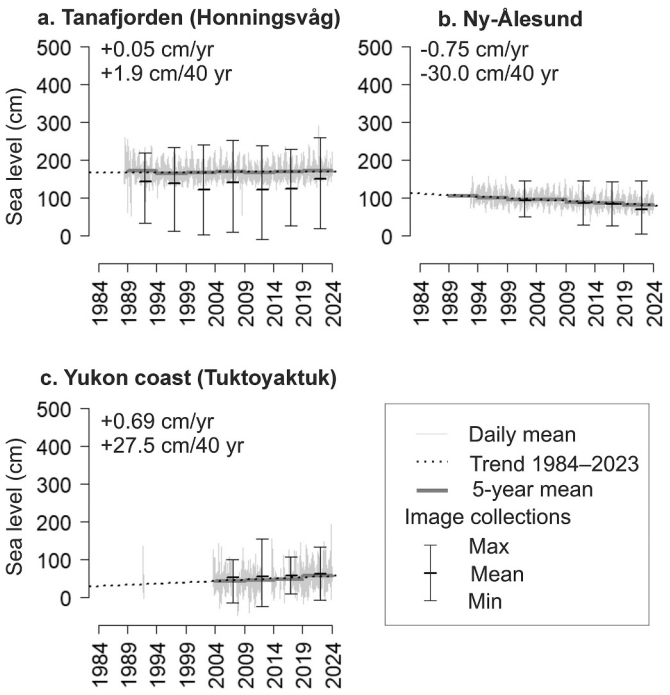

Fig. 11. Sea level patterns in the three calibration sites. Panel a. shows sea level data for the Tanafjorden calibration site, panel b. for Ny-Ålesund, and panel c. for Yukon coast. All sea levels are given relative to the local chart datum. The charts present daily mean time-series, linear trend during 1984–2023, and mean sea level during each five-year time-step, as well as the lowest, median, and highest sea level at the acquisition time of satellite images (for images with a sea level observation taken <2 h before or after the image acquisition time). Data: Norwegian Hydrographic Service, API for water level data (https://api.sehavniva.no/tideapi_en.html); Fisheries and Oceans Canada, Canadian Tides and Water Levels Data Archive (https://www.isdm-gdsi.gc.ca/isdm-gdsi/twl-mne/index-eng.htm).

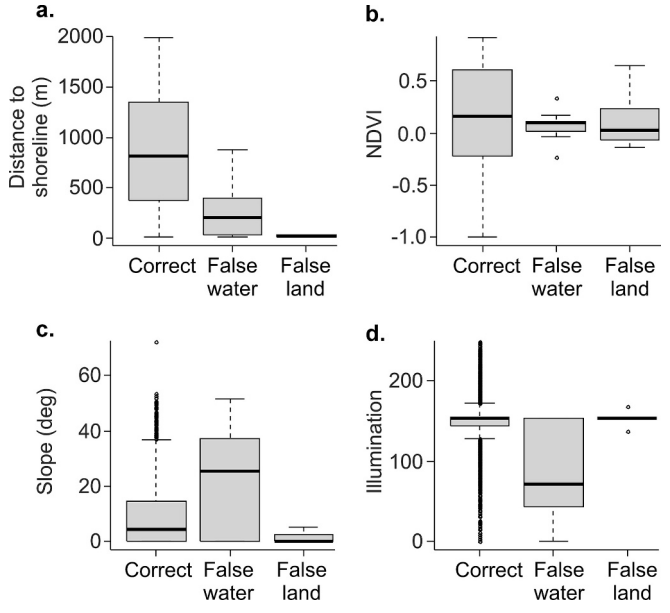

Fig. 12. Impact of local environmental conditions on classification accuracy. Panel a. shows classification accuracy in the Tanafjorden calibration site in 2019–2023 in areas of varying distance to shoreline, panel b. with varying primary productivity (measured with normalized difference vegetation index NDVI), panel c. with varying terrain slope and panel d. with varying illumination conditions.

calibration site, we saw that water and ice points with similar NDWI values could be reliably separated from each other using a Landsat level 2 NIR band threshold of 10,000 (Fig. 7). Accordingly, we used the following NDWI and NIR (level 2) pixel value thresholds for separating land, water, and ice (or snow) pixels:

- land: NDWI $\leq$0
- water: NDWI >0 and NIR < 10,000
- ice: NDWI >0 and NIR $\geq$ 10,000

After applying this land-water-ice classification in the Landsat 8 land cover dataset for 2019–2023, 1052 out of 1056 true water points were correctly assigned to the water class, and 110 of the 120 true ice points to the ice class (Table 6). The remaining classification errors were concentrated at the shoreline and at the margin of the marine-terminating glaciers (Fig. 8b). They were mainly misclassified because of mixed pixels, and the small movement of the glacier margin. A notable number of remaining classification errors were also concentrated on steep slopes, where shadow effects have a high impact on reflectance (Fig. 8b). We ensured that the same threshold would be applicable to Landsat 5 and Landsat 7 images by repeating the analyses for these sensors and earlier time-steps (Supplementary Fig. S4 and Table S4).

4.1.6. *Decision fusion over time-steps*

The land-water-ice classification results based on a single highest-quality Landsat image in the Tanafjorden calibration site were outperformed by decision fusion (or composite) results in the Tanafjorden calibration site (Table 7). That is, the post-classification mode composite over all suitable images for a five-year time-step provided higher overall accuracy and higher Kappa values for the time-step 2019–2023 (Table 7). In addition, the number of missing value pixels due to, e.g., cloud cover was reduced from 9 % in the single highest-quality image to less than 0.1 % when using the composite (Table 7). The repeated analysis for the time-step 1984–1988 supported the use of the decision fusion (Supplementary Table S5). Thus, summarizing data over time-steps supported the aim to produce a homogeneous coastal land cover dataset that reflected longer-term changes rather than short-term fluctuations.

The pre-selected time-step length of five years seemed optimal based on data availability analyses. In the Tanafjorden calibration site, most pixels had at least ten valid, cloud-free observations per all five-year time-steps except 1994–1998 (Table 8). During the problematic time-step 1994–1998, c. 11 % of the pixels lacked the minimum number of valid observations and were considered missing data in the land cover dataset (Table 8). From this time-step onwards, the number of observations increased gradually (Table 8).

In the Ny-Ålesund calibration site, data availability varied notably through time (Table 8). There was in practice no valid data for 1984–1988, and little for 1994–1998 (Table 8). Also, during 2004–2008 there were c. 32 % of pixels with insufficient number of valid observations (Table 8). Thus, the time-series was in practice 35 years long with gaps in 1994–1998, and 2004–2008. Until 2014–2018, data availability was in general lower than in the other calibration sites (Table 8).

In the Yukon coast calibration site, data availability in 1984–1988 was slightly lower than in Tanafjorden, but notably higher for the rest of the time-series (Table 8). From 2004–2008 onwards, the entire calibration site, in practice, had more than 30 valid observations per pixel and time-step (Table 8).

Since the number of pixels with less than 10 valid observations per five-year time-step was notable in all calibration sites for at least one time-step (Table 8), we concluded that it was not realistic to consider dividing the time-series into shorter time-steps. In the Tanafjorden calibration site, shortening the time-step to four or three years would have notably increased the number of missing data pixels in the 1990s, but not affected data availability otherwise (Fig. 9). A shortening to two

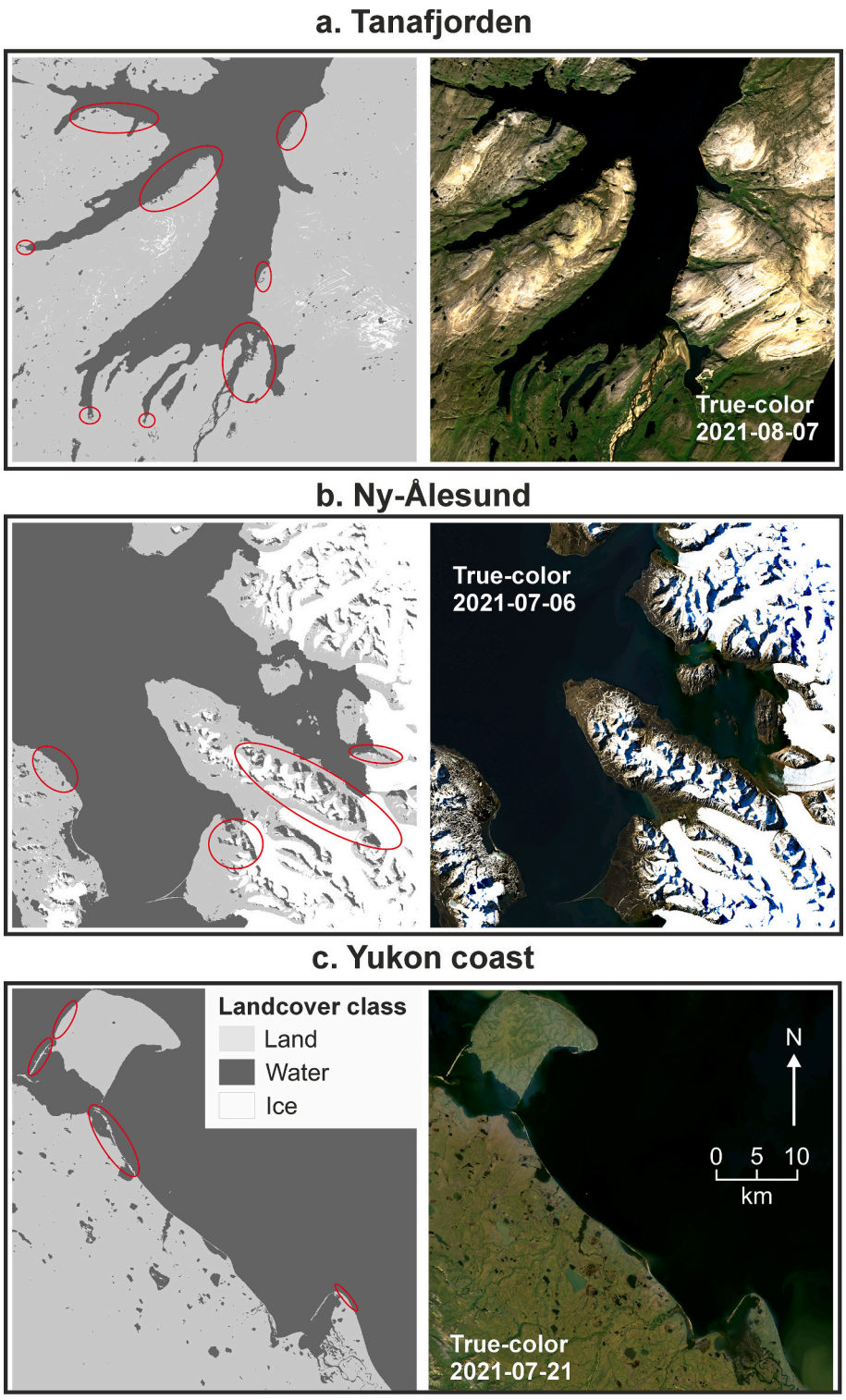

Fig. 13. Land cover and problematic areas after simple threshold-based classification. Panel a. shows land cover classification results based on NDWI and NIR thresholds in 2019–2023 in the Tanafjorden calibration site, panel b. in Ny-Ålesund and panel c. in the Yukon coast. Example areas with notable classification problems are circled on the land cover maps. True-colour Sentinel-2 images are shown for reference.

years would have, in practice, created a 10-year-long gap in the time-series in the 1990s (Fig. 9). One-year time-steps would not have had enough data for the composite approach until 2015, as more than 50 % of the pixels had less than five observations per year for most of the years (Fig. 9).

When applying the five-year composite approach to the entire Arctic, the extracted time-series consisted of eight time-steps in 71 % of the coast (Fig. 10). For more than 97 % of the coastal zone, the time-series consisted of at least five time-steps (Fig. 10). The spatial distribution of the number of time-steps reflects the date of the first available image, and the number of individual images (compare Fig. 10 and Fig. 3). The time-series begins later than 1984 in southern and northern Greenland, Ellesmere, western Alaska, eastern Siberia, and Svalbard (Fig. 10). This was the case also in the small, isolated islands, including Faeroe Islands,

Table 9
Classification results in the Tanafjorden calibration site in 2019–2023 in areas with different substrate.

	Correct	False water	False land	False (%)
Bedrock	1136	13	3	1.4
Gravel	114	0	2	1.8
Sand	38	3	2	13.2
Deep sea	678	0	0	0.0

Table 10
Accuracy of original, random forest and composite classifications. The table presents the accuracy of the original land cover classification (based on NDWI and NIR thresholds), random forest classification, and the composite classification based on independent validation point data in 2019–2023 in the Tanafjorden (panel a.), Ny-Ålesund (panel b.) and Yukon coast (panel c.) calibration sites. The highest overall accuracy for each calibration site is highlighted with bold text.

a. Tanafjorden 2019–2023			
Model version	Original	Random forest	Composite
Overall accuracy	98.9	97.7	**99.3**
Kappa	0.976	0.952	0.984
b. Ny-Ålesund 2019–2023			
Landsat product	Original	Random forest	Composite
Overall accuracy	97.2	80.2	**98.2**
Kappa	0.949	0.652	0.966
c. Yukon coast 2019–2023			
Landsat product	Original	Random forest	Composite
Overall accuracy	**99.2**	99.1	**99.2**
Kappa	0.983	0.982	0.983

Jan Mayen, Bear Island (Bjørnøya), White Island (Kvitøya), Victoria Island, and Ushakov Island, where very low data availability in practice prevented change detection (Fig. 10). For example, the time-series mainly consists of 2–3 time-steps in Faeroe Islands, 1–2 time-steps in the Bear Island, and one time-step in the Ushakov Island (Fig. 10).

4.1.7. Impact of sea level trend and tide on shoreline position

Relative mean sea level in the Tanafjorden calibration site was stable during the period 1988–2023 (Fig. 11a), suggesting that all shoreline changes detected in our study were caused by short-term fluctuations in sea level, erosion, sediment deposition or anthropogenic impacts. In the Yukon coast, the relative sea level was rising in 2003–2023 (Fig. 11b), indicating that sea level rise and land subsidence should have caused landward retreat of the shoreline, even without erosion. The relative sea level was dropping in Ny-Ålesund (Fig. 11b) due to post-glacial rebound, which could have led to seaward progression of the shoreline during the examined 40 years even without sediment deposition.

The Landsat image acquisition time sea levels covered, in practice, the entire range of short-term sea level fluctuations in the four examined calibration sites (Fig. 11). Thus, without external tide gauge data, high-quality bathymetric and elevation data and tidal corrections, results based on single images would have made coastal land cover time-series highly vulnerable to sea level differences. When comparing the mean of Landsat image acquisition time sea levels over each five-year time-step to the long-term sea-level trend, we were able to assess if the time-step composite was likely to represent mean summer-time sea level conditions. Both random factors and seasonality caused that the mean Landsat image sea level (in summer months) deviated from the annual sea level trends, but an order of magnitude less than single-image sea levels (Fig. 11).

In the Tanafjorden and Ny-Ålesund calibration sites, the Landsat images were throughout the time-series acquired when the sea level was lower than in average (Fig. 11a-b). This at least partly reflected seasonal patterns, with sea level being generally lower during summer around Tanafjorden and Ny-Ålesund. The deviation is notably larger in the Tanafjorden calibration site than in Ny-Ålesund, due to higher tidal amplitude (Fig. 11a-b). The largest deviance in all examined calibration sites was 47 cm in Tanafjorden in 1999–2003 (Fig. 11a). In Tanafjorden, the means of Landsat image acquisition time sea levels were c. 20 cm lower during time-steps 1999–2003, 2009–2013 and 2014–2018 than during other time-steps (Fig. 11a). In the Ny-Ålesund calibration site, the mean of Landsat image acquisition times clearly deviated from the trend during 2019–2023, being c. 14 cm lower than the long-term average (Fig. 11b). In the Yukon coast calibration site, the mean of Landsat image acquisition time sea levels was higher than the long-term mean sea level, with a 5–11 cm deviance (Fig. 11c). Undoubtedly, these remaining differences between time-steps might have influenced the location of the extracted shoreline, particularly in flat meso-tidal areas like the Tana River delta.

4.1.8. Classification challenges due to local conditions

Based on visual inspection of the classification results for the time-step 2019–2023, the land-water-ice classification based on NDWI and NIR thresholds resulted in relatively accurate coastal land cover detection. The most distinct classification errors, not merely caused by mixed pixels and random factors, were identified at the steep north-facing slopes. The next iteration (chapter 4.1.9) concentrated on reducing their classification errors.

In the mountainous Tanafjorden calibration site, majority of the remaining classification errors were concentrated on steep, north-facing cliffs with many false water detections, and in the flat intertidal areas (Fig. 12, Fig. 13a). Closer examination of the classification errors showed that the false water detections (land classified as water) were located close to the shoreline, but there were false detections also several hundred meters away from the shoreline (Fig. 12a). Many of the problematic areas were bedrock hillsides (Table 9) with higher terrain slope (Fig. 12a) and receiving less illumination than on average (Fig. 12d). The false land detections were in practice concentrated in flat areas along the shoreline (Fig. 12a, c), many of them gravel or sand beaches (Table 9), reflecting the impacts of mixed pixels and tidal sea level variation. Reducing errors related to mixed pixels and tidal variations in the extremely flat intertidal areas even further was beyond the scope of this study.

In the Ny-Ålesund calibration site, most of the remaining classification errors were also concentrated in mountain shadows (Fig. 13b). At the gently sloping Yukon coast, there were generally few classification errors (Fig. 13c). Notably, however, the wave-exposed coastlines of Ny-Ålesund and Yukon were in many places bordered by ice in the land cover results (Fig. 13b-c). This either reflected the prolonged presence of pack ice on the shores in the summer or indicated that the NIR threshold applied in the classification was too low, causing pixels of breaking waves to shift from the water class to the ice class.

4.1.9. Improving classification in mountain shadows

Based on the results, random forest classification with existing land cover and topographic data resulted in a lower overall accuracy than the original classification based on NDWI and NIR thresholds in the three calibration sites (Table 10). However, the random forest classification performed better in mountainous coasts, more often separating mountain shadows correctly from water than the original classification. Thus, when the final land cover layer was generated as a composite from the original class for gently sloping and sunlit areas, and from the random forest class in areas with mountain shadows, the classification accuracy improved (Table 10). The improvement was notable in the mountainous Tanafjorden and Ny-Ålesund calibration sites (Table 10a-b; Fig. 14a-b). In the gently sloping Yukon coast, however, there was no improvement from the original classification, as problems with mountain shadows were negligible in this area (Table 10c; Fig. 14c).

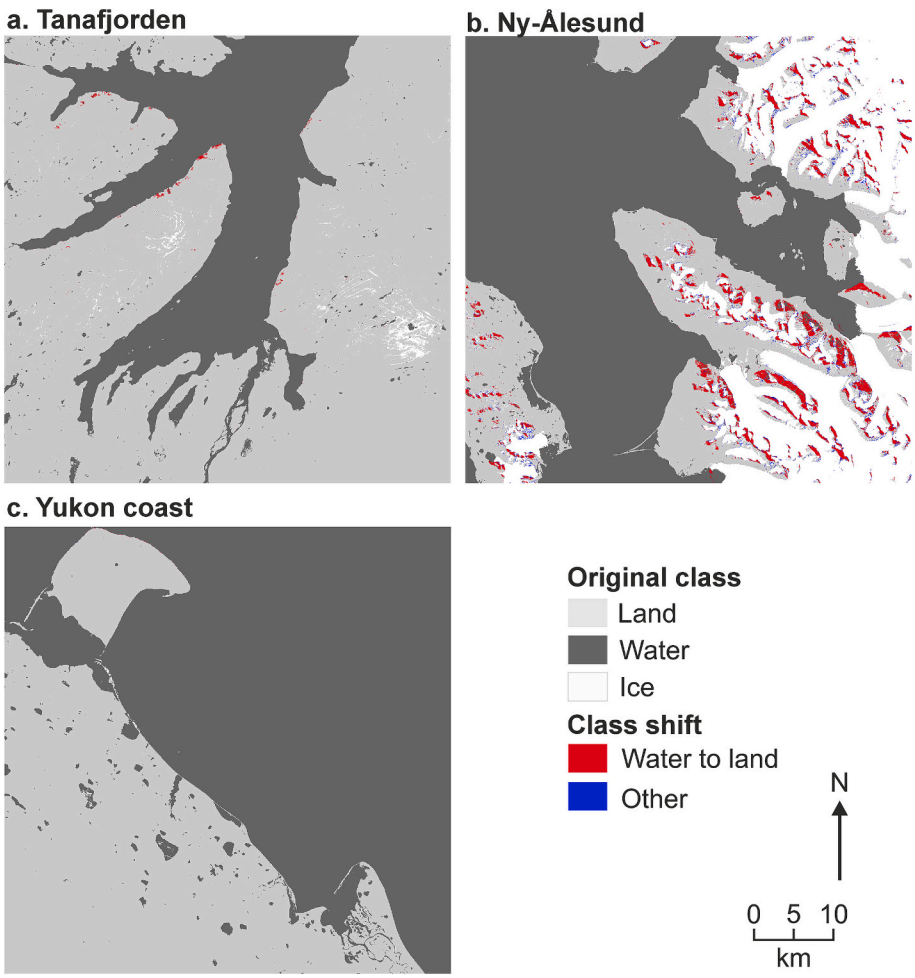

Fig. 14. Distribution of pixels that shift land cover class when applying the random forest algorithm on areas with hill shadows. The results for 2019–2023 are shown for the calibration sites of Tanafjorden in panel a., Ny-Ålesund in panel b., and Yukon coast in panel c.

Table 11
Land cover classification accuracy and shoreline error distances of the final procedure for the time-step 2019–2023. Classification accuracies are examined against the independent set of 2000 coastal points in each calibration site.

	Tanafjorden	Ny-Ålesund	Yukon coast
Overall accuracy	99.3	98.2	99.2
Water points classified as land	9 (1.1 %)	0 (0.0 %)	3 (0.3 %)
Land points classified as water	6 (0.5 %)	13 (1.6 %)	7 (0.8 %)
Errors involving ice class	–	24	6
Shoreline transects	10,424	6556	5438
Median error distance (m)	20.8	9.2	9.2
95 % quantile error distance (m)	51.0	29.6	33.6

4.2. Produced Arctic coastal change data

4.2.1. Structure of the new dataset

The presented Arctic Coastal Change dataset consists of eight time-steps, 1984–1988, 1989–1993, 1994–1998, 1999–2003, 2004–2008, 2009–2013, 2014–2018 and 2019–2023, and can be in the future supplemented with following time-steps like 2024–2028. The dataset consists of two types of data, coastal land cover and number of observations on each pixel. Pixels with less than five valid observations during the time-step are classified as missing data. The dataset covers the coastal zone of the entire study area (Fig. 1), excluding the northernmost tip of Greenland that did not have Landsat observations (Fig. 3). To keep file sizes manageable, the dataset consists of 23 large tiles.

4.2.2. Accuracy of the final coastal land cover classification

Validation of the coastal land cover outputs for the time-step 2019–2023 against the independent set of 2000 coastal points showed, that the procedure reached an overall classification accuracy of over 98 % in all three calibration sites (Table 11). There were more misclassified water points in Tanafjorden and more misclassified land points in Ny-Ålesund and Yukon coast (Table 11).

In most cases, those land points that were misclassified as water and those water points that were misclassified as land were located very close (in practice all less than 30 m) to the actual shoreline (Fig. 15a–c). In Tanafjorden, there were classification errors also in intertidal zones and in areas shadowed by mountains (Fig. 15a). In the Ny-Ålesund calibration site, classification errors concentrated in areas with highly dynamic spits (Fig. 15b). There were also classification errors related to the ice class (Fig. 15b), but these did not affect the conclusions on shoreline displacement. In the Yukon coast, classification errors also concentrated in areas of dynamic spits and lagoons (Fig. 15c).

The median error distance from the reference shoreline to the modelled shoreline was less than 25 m in all three calibration sites, i.e., less than the Landsat image pixel size of 30 m (Table 11). In Tanafjorden, the longest error distances were found either in intertidal zones – most of them located in estuaries – or in mountain shadows (Fig. 15d). The median error distance was even shorter than in Tanafjorden, less than 10 m, in the Ny-Ålesund and Yukon coast calibration sites (Table 11). In Ny-Ålesund, the longest error distances mainly occurred in ice-marginal areas and along spits, but some also in the lagoon of Richardlaguna on the island of Prins Karls Forland and at a pier in the town of Ny-Ålesund

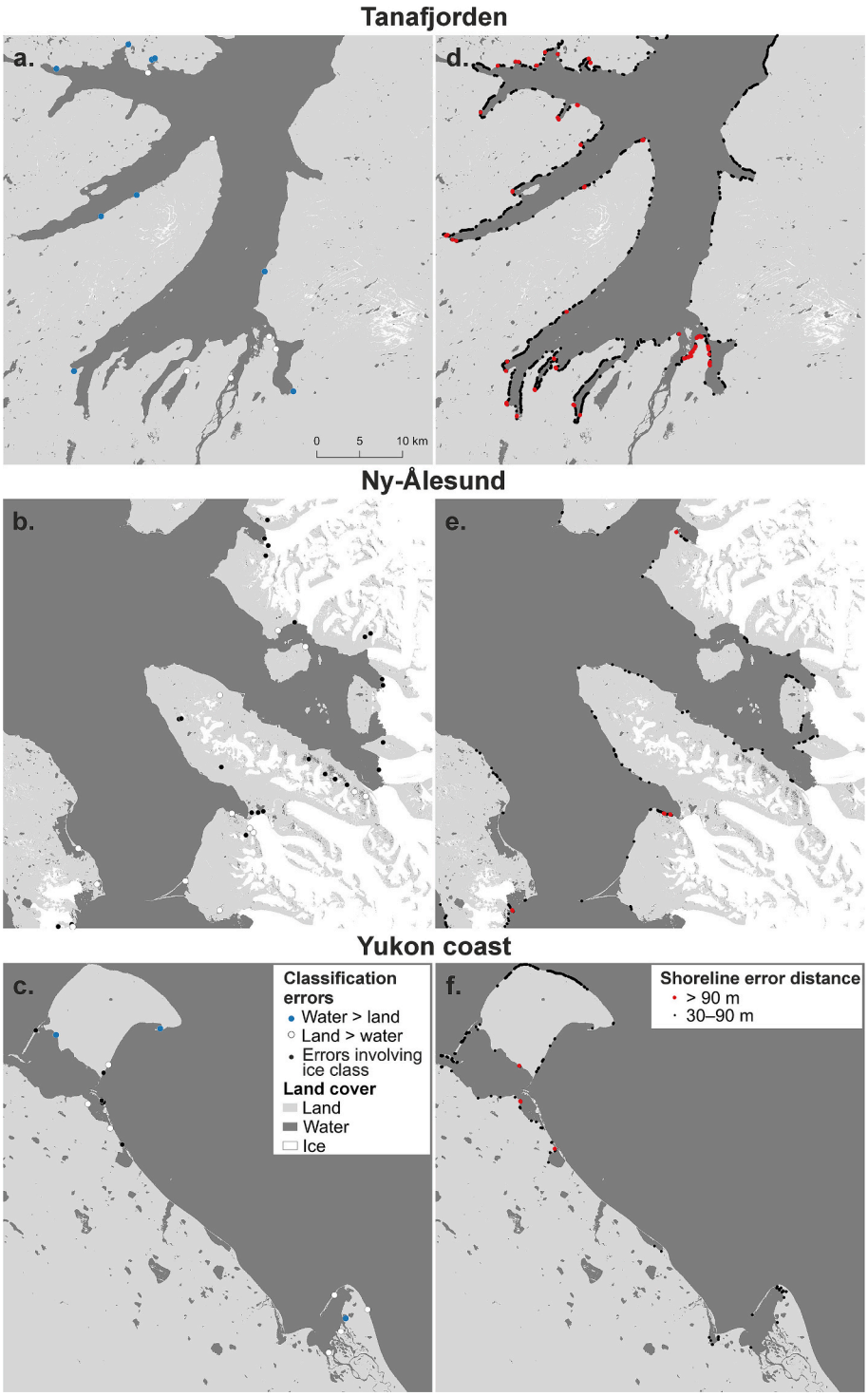

Fig. 15. Distribution of errors in the final coastal land cover data. Panels a.–c. show the distribution of the misclassified reference points and panels d.–f. the shoreline error distances for the time-step 2019–2023 in the three calibration sites.

(Fig. 15e). In the Yukon coast, the longest shoreline error distances were found along spits around the Herschel Island, in coastal lagoons, and in the dynamic Babbage River delta (Fig. 15f).

4.2.3. Correspondence of calculated shoreline change rates and previous studies

Comparison of the modelled and reference erosion and accretion rates for the 61 validation sites showed a general correspondence (Fig. 16, Fig. 17a–b; Supplementary Table S6). Of the 61 sites, both modelled and reference rates indicated coastal erosion in 43 sites and there was a significant positive correlation of erosion rates ($p < 0.01$; Fig. 16a). Similarly, modelled and reference rates indicated coastal accretion in 5 sites (Fig. 16b).

The modelled and reference rates disagreed on the direction of shoreline change in 13 sites (Fig. 16c). However, all these rates were close to zero (modelled rates from −0.16 to 0.52; Fig. 16c), indicating that they were stable coasts. Considering the Landsat pixel size of 30 m, the limit of detection during a 40-year period is c. 0.375–0.75 m per

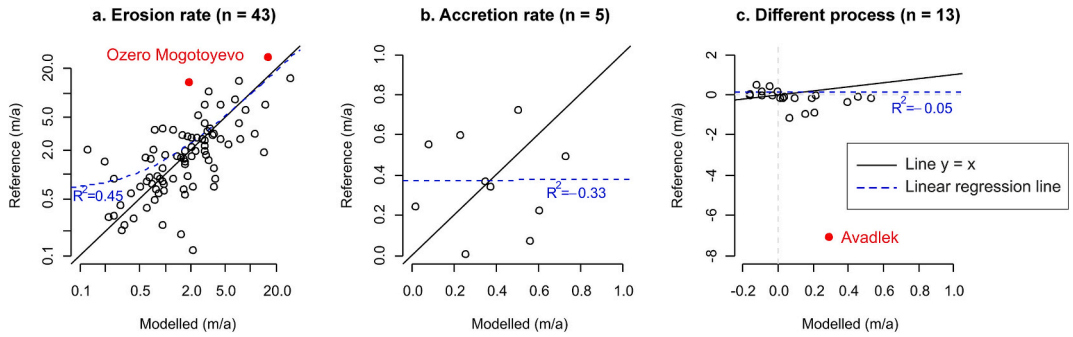

Fig. 16. Comparison of modelled and reference shoreline change rates for 61 validation sites. The figure is divided into cases where both indicate erosion (panel a.; note reversed logarithmic scales) or accretion (panel b.), and cases where our results and the reference rates indicate opposite trends (panel c.). In panel c. negative rates indicate erosion. Note that the time frame of the change rates varies between validation sites. The largest discrepancies in Ozero Mogotoyevo in the Russian East Siberian Sea coast (a.; c.f. Wang et al., 2022) and Avadlek in the western coast of Herschel Island in the Canadian Beaufort Sea coast (c.; c.f. Bartsch et al., 2020) are highlighted. The distribution of the validation sites is shown in Fig. 1e. See Supplementary Table S2 for a table of the results.

year. All 13 rates deviated from zero less than 0.75 m per year (Fig. 16c). In addition, the shoreline change envelope, i.e., the mean distance of shoreline changes for these sites for the examined period ranged from 5.2 to 56 m, being less than 30 m in nine of them (Supplementary Table S6).

The most distinct discrepancies between our model and previously reported rates were found in Ozero Mogotoyevo in the Russian East Siberian Sea coast (Fig. 16a; c.f. Wang et al., 2022) and in Avadlek in the western coast of Herschel Island in the Canadian Beaufort Sea coast (Fig. 16c; c.f. Bartsch et al., 2020). The data of Wang et al. (2022), based on satellite radar data, indicate extremely high erosion rates of 14 and 28 m per year in 1992–2017 in two Ozero Mogotoyevo sites, whereas our data suggested slower erosion rates of 1.9 and 16 m per year during the corresponding period 1999–2003 to 2014–2018. One source of difference may have been that the period examined by us was shorter due to a lack of Landsat data in the area before 1999. The satellite radar-driven data of Bartsch et al. (2020) indicate rapid retreat of the Avadlek coast of −7.0 m per year in 2007–2018, while our data indicate that the coast was stable during the corresponding period 2004–2008 to 2014–2018 (0.3 m per year; Fig. 16c; Supplementary Table S6).

5. Discussion

5.1. Interpreting the Arctic Coastal Change data at different scales

The added value of the new Arctic Coastal Change dataset (Nylén, 2024) is that it allows researchers to identify coastal change hotspots across the Arctic at different scales, i.e., global, regional, and local scale. It serves as a spatially consistent medium-resolution baseline dataset, that can be used, for example, to support trend analyses over the past 40 years and for future projections (like that of Nielsen et al., 2022). Unlike the previous coastal erosion dataset by the Arctic Coastal Dynamics consortium (Lantuit et al., 2012), our dataset has a circumpolar coverage, also including the Canadian Arctic Archipelago, Greenland, and the coast of the Norwegian Sea. It also covers a much longer period than other datasets, such as that of Philipp et al. (2023). Such data can provide essential information for regional administration and local communities to better adapt to the impacts of climate change in these vulnerable regions. The dataset opens new possibilities for Arctic coastal dynamics studies across scales.

Traditionally, coastal dynamics have been visualized with vector data, by assigning erosion rates to coastal points or coastline segments (cf. Lantuit et al., 2012; Philipp et al., 2023). However, coastal dynamics can also be examined with a multitemporal raster dataset using change detection methods and calculating time-series summary layers. These can be, for example, net change between the first and last observation or the last time-step in the land class, indicating the timing of permanent loss of land. Our Arctic Coastal Change viewer (link) in Google Earth Engine can be used for examining net land cover change and the timing of the permanent loss of land or water across the Arctic. It also allows exploration of the full coastal land cover time series flexibly at different scales.

Our approach allows locating global-scale coastal erosion and accretion hotspots in the Arctic. Based on a preliminary examination and postprocessing of the Arctic Coastal Change data, a notable proportion of the coastline, c. 8 % of the sampled locations, is experiencing rapid coastal erosion or rapid coastal accretion of more than ten meters per year (Fig. 18; Arctic Coastal Change viewer). Erosion hotspots can be found, for example, in the northern coast of Alaska, Yukon, and Northwest Territories, Hudson Bay and Russian federal subjects of Nenets, Yamalo-Nenets, Krasnoyarsk, and Sakha (Fig. 18). The rocky coasts of Newfoundland, western Greenland, Iceland, Norway and Novaya Zemlya, for example, are shown to have been relatively stable during the past decades.

These global erosion hotspots can be further examined in the Arctic Coastal Change viewer, showing extreme permanent loss of land along many headlands and river deltas of the coasts of Alaska and mainland Canada (e.g., Bering Land Bridge National Preserve, Point Lay, Drew Point, Yukon coast, and MacKenzie River Delta). Further North American erosion hotspots are found along the northwestern coast of Prince Patrick Island, the coasts of Roes Welcome Sound, and in Ungava Bay. In the Russian arctic, erosion hotspots can be found, for example, from the headland of Mezen in the White Sea, Kanin Peninsula and Pechora Sea coast in the Barents Sea, Baydaratskaya Bay and the Pyasina river delta in the Kara Sea coast, Lena Delta in the Laptev Sea coast, and the coasts of Bolshoy Lyakhovsky Island, Dmitry Laptev Strait and Cape Maly Chukochy in the East Siberian Sea (see example site menu in the Arctic Coastal Change viewer).

Hotspots of coastal accretion are spatially much more restricted than erosion hotspots. Accretional coasts are most common in areas with high rates of postglacial land uplift, namely northeastern Canada, Greenland, Iceland, Norway, Svalbard and Novaya Zemlya (Fig. 18). Examples of larger accretion hotspots can be found in North America in the coasts of Eschscholtz Bay in western Alaska, in the spits of Peard Bay, Point Barrow and Canning River delta in the Alaska North Slope, and in the Canadian coasts with high post-glacial land uplift rates like southwest Baffin Island and Port Nelson in the Hudson Bay (see example site menu in the Arctic Coastal Change viewer). In the Russian Arctic, accretion hotspots can be found, for example, in the White Sea coasts of Olenitsa and southern Kanin Peninsula, as well as in Chernaya in the southern Barents Sea coast and northeastern Taymyr Peninsula (see example site menu in the Arctic Coastal Change viewer).

Notably, the regional and local-scale variability in coastal dynamics is evident also when examining the results at the global scale. This

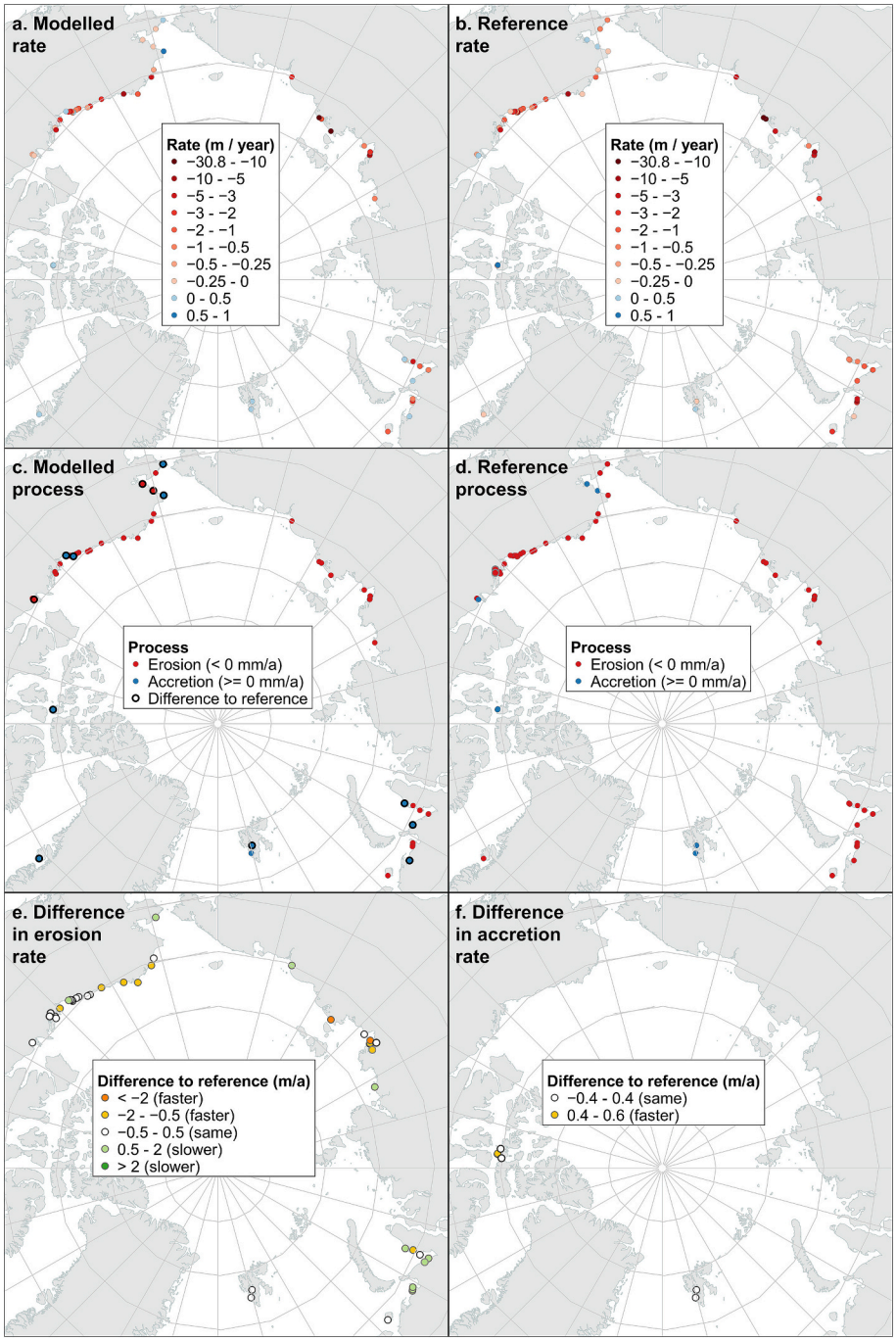

Fig. 17. Distribution of modelled and reference shoreline change rates for 61 validation sites. Panels a. and c. show modelled and panels b. and d. reference end-point-rates for the 61 validation sites. Negative rates indicate erosion. Panel e. compares erosion rates and panel f. accretion rates between the model and the reference. Note that the time frame of the change rates varies between validation sites. See Supplementary Table S2 for a table of the results.

observation highlights the value of being able to work with a homogeneous raster dataset across scales zooming in to potential erosion hotspots, for example.

The spatial resolution of the Arctic Coastal Change dataset (Nylén, 2024) is 30 m, corresponding to the resolution of the Landsat time-series. This can be considered a sufficient resolution for examining some of the most distinct regional-scale processes in the Arctic, such as coastal erosion, land subsidence, the development of deltas and barrier islands, as well as glacier retreat. Taking the Bykovsky Peninsula as an example, the regional-scale patterns in erosion rate can be clearly seen in the Arctic Coastal Change dataset (Fig. 19). The Bykovsky Peninsula is located in the Russian Laptev Sea coast near the settlement of Tiksi, and its coastal dynamics have been studied, e.g., by Lantuit et al. (2011), Bartsch et al. (2020), and Nielsen et al. (2020). As suggested by previous studies, our data confirm that most of the coastline has been erosional since 1999 (Fig. 19). The area of eroded land between time-steps 1999–2003 and 2019–2023 (Fig. 19a) is c. 14.6 km^2 or almost 0.5 % of the area of Fig. 19.

Compared to what was observed by Lantuit et al. (2011) in the early 2010s, many previously stable or accretional coastal sections of the Bykovsky Peninsula have become erosional, and erosion rates have increased up to almost 9 m/a (Fig. 19). The mean erosion rate for the area has increased from 0.59 m/a in 1951–2002 (Lantuit et al., 2011) to 1.21 m/a in 1999–2023. Erosion rates are in general highest in the

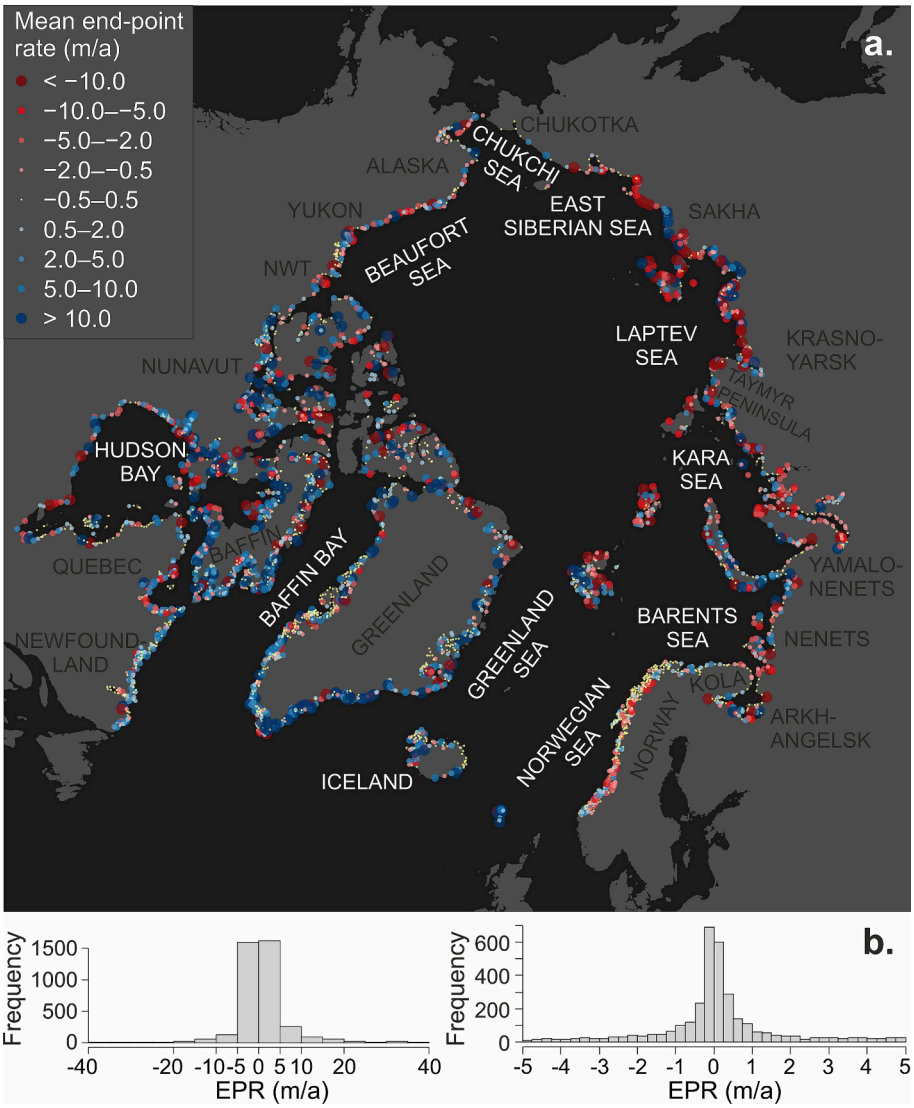

Fig. 18. Global-scale distribution of preliminary shoreline displacement rates. Panel a. shows the circumpolar distribution of preliminary shoreline change end-point rates in 1984–2023, calculated for a sample of 4106 coastline sections with DSAS (Himmelstoss et al., 2024). Panel b. shows the frequency distribution of end-point rates in these 4106 sites.

central parts of the peninsula, while accretion is localized in areas close to the settlement and airport of Tiksi and the northern tip of the peninsula facing the Lena River Delta (Fig. 19b; c.f. Lantuit et al., 2011). Three highly localized erosion hotspots with rates exceeding 6 m/a can be identified at the east coast of the peninsula (Fig. 19b). These same three hotspots were highlighted also by Lantuit et al. (2011).

Within the limits of the 30-m resolution, the local-scale differences in shoreline dynamics are also clear in the Arctic Coastal Change dataset, at least in areas with notable erosion and accretion patterns. We take an example from the coasts of Point Hope in the Alaskan Chukchi Sea coast (Fig. 20). In 1999–2023, the mean shoreline change rate was 0.47 m/a, indicating that the coast is in general stable or slightly accretional. However, the local differences are notable. In 1999–2023, 32.6 ha of land eroded, and 41.3 ha of new land formed (Fig. 20a). Erosion rates exceeded 1 m/a at the north-western tip of Point Hope very close to the airport (Fig. 20b), as also reported by Gibbs et al. (2019). Accretion rates exceed 1 m/a along most of the southern coast of Point Hope, where also the settlement is located (Fig. 20b). This is also in accordance with the findings of Gibbs et al. (2019).

The Arctic Coastal Change dataset also allows examination of the temporal patterns in coastal dynamics with a five-year precision. Examination of the data reveals that coastal erosion at one of the hotspots in the Bykovsky Peninsula was gradual and unidirectional during the examined period 1999–2023 (insert in Fig. 19a). The shoreline retreated c. 200 m in the north-western and central parts of the section seen in the insert in Fig. 19a during the 20-year period, with relatively uniform pace. The erosion hotspot at the tip of Point Hope has experienced much less erosion, mainly c. 50–100 m during the 20-year period (Fig. 20a). Thus, the changes between successive time-steps generally fall under the limit of detection of our method. However, the data suggest, that majority of erosion of the tip of the headland occurred already between 1999 and 2003 (Fig. 20a).

5.2. *Challenges and future development*

Like any method, our procedure it is not without challenges and limitations. The following section discusses the main challenges and development needs identified during the project and preliminary examination of the new global Arctic Coastal Change dataset (Nylén, 2024). As the area is diverse, solving both the technical challenges and the challenges caused by environmental factors for next versions of the dataset may be a collaborative effort in the future.

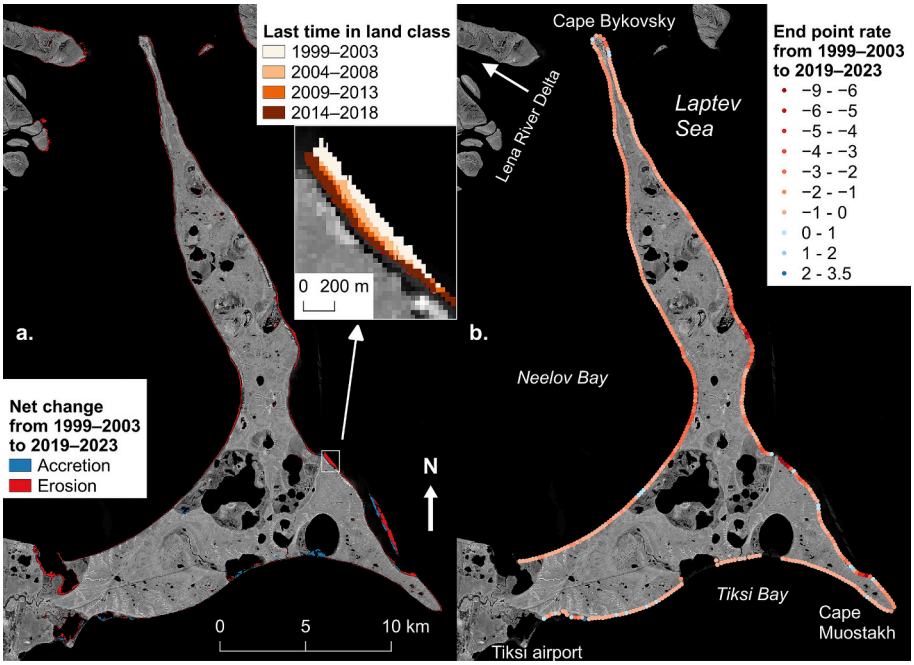

Fig. 19. Regional-scale example of coastal dynamics. Panel a. shows the regional-scale distribution of coastal change and panel b. the shoreline change rate along the coast of the Bykovsky Peninsula in the Russian Laptev Sea coast. Negative rates indicate erosion. Compare to, e.g., Lantuit et al., 2011 (their Fig. 8 in particular) for previously documented erosion rates. Change rates have been calculated with DSAS software (Himmelstoss et al., 2024) from the original Arctic Coastal Change dataset (Nylén, 2024). Background: Copernicus Sentinel-2 NIR image from 17.8.2020.

Masking of bad pixels in individual satellite images is in our procedure based on the Landsat pixel quality band. This information is not perfect, and we have identified a tendency for the white-water zone of exposed sand and gravel beaches to be falsely detected as clouds and masked from the image. This phenomenon has created some narrow data gaps along the shoreline. In a few (mainly remote and dynamic) locations, the automatically calculated four-kilometre-wide coastal zone does not overlap with the coastline. This problem, inherited from the OpenStreetMap coastline product, has resulted in localized gaps in the data. These technical challenges may be in the future dealt with, for example, by applying more sophisticated pixel quality algorithms and better-suited shoreline datasets. Moreover, low data availability in the remote high latitude areas during the 1980s and 1990s tends to create local gaps in the time-series, and results in relatively low classification accuracy in areas with very few (e.g., 5–10) observations on each pixel. While data availability cannot be increased, we may revisit the threshold of the number of valid observations or use complementary spatial data to filter the land cover dataset.

The coastal environments of the Arctic are diverse. In the Arctic Coastal Change dataset, the main classification challenges caused by natural environmental variability and local conditions, such as summer ice, steepness of the coast, shadows, sea level changes and tidal variation, have been accounted for. Although the methodology is widely applicable, there are still areas with specific environmental conditions where the output land cover data are not accurate enough for reliable coastal change analyses. For example, it appears that some pixels of the white-water zone of wave-exposed coasts have been falsely classified as ice in the land cover data. This narrow belt of ice class pixels complicates automated shoreline extraction. In the future, the ice threshold could be revisited, and other spectral bands and complementary data sources could be utilized to improve the classification of the white-water zone.

While one globally applied seasonal time window from June to September suites many Arctic coasts and ensures that many June images with good illumination conditions are included in the dataset, in specific areas sea ice cover in June and September images causes problems. Notable sea ice cover may decrease classification accuracy and visibility of the land-sea-interface, with consequences for coastal change applications. In the next versions of the dataset, we will consider the use of local or image-specific filtering criteria and an updated time-step compositing strategy to reduce the impact of sea ice.

Despite efforts to reduce the impact of mountain shadows on the coastal land cover classification, there remain steep fjord coasts with notable classification problems, particularly during the time-steps of the 1980s and 1990s. In fjord coasts of southern Norway, southwestern Greenland and many Arctic islands, the sharp contrasts between sunlit mountain slopes and mountain shadows still complicate the classification of land and water, particularly during time-steps with a limited number of Landsat observations. We believe that these errors can be removed with appropriate use of complementary spatial data, potentially including SAR imagery, and targeted filtering of the initial land cover data. For example, we may use image-specific solar angle information when filtering imagery, excluding images with very low solar angles and highly oblique illumination, or apply a seasonal time window that varies with latitude. Also, other natural processes can be considered for improving the procedure in the future. For example, suspended sediment present in intertidal and coastal waters next to river mouths still cause local classification problems.

6. Conclusions

Spatially consistent baseline data on past Arctic coastal dynamics are urgently needed to help inform local communities and regional administration on how the coast is expected to change in the next decades. In this paper, we introduce a high-performance procedure for mapping coastal land cover dynamics from satellite images in the challenging Arctic conditions. We also demonstrate the capabilities of the procedure in the Arctic. The procedure is built in a way that it can also be applied to environments beyond the Arctic, for providing new information on coastal erosion and accretion in boreal, subtropical and tropical regions.

Our approach utilizes the full Landsat satellite collections and complementary spatial data for accurate and efficient coastal land cover

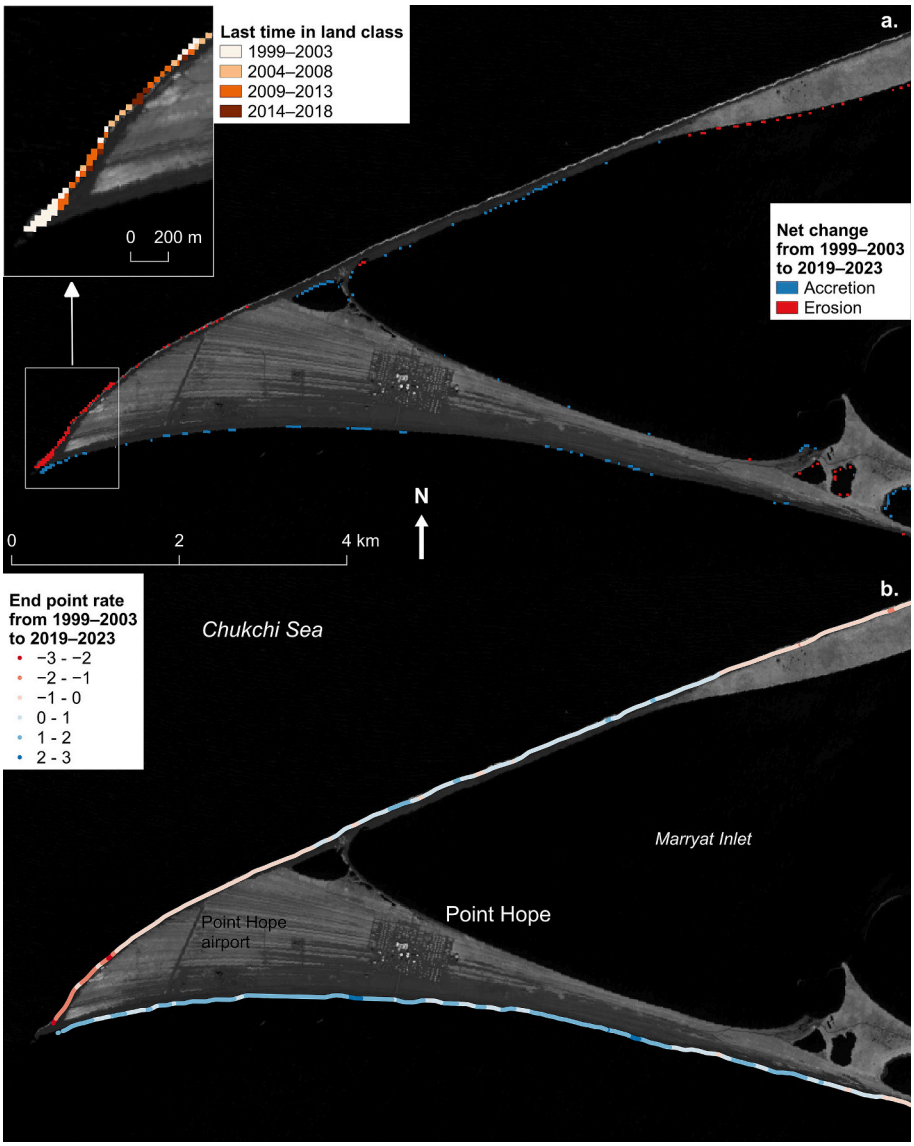

Fig. 20. Local-scale example of coastal dynamics. Panel a. shown the local-scale distribution of coastal change and panel b. the shoreline change rate around the community of Point Hope in the Alaskan Chukchi Sea coast. Negative rates indicate erosion. Compare to, e.g., Gibbs et al., 2019 (their Fig. 18 in particular) for previously documented erosion rates. Change rates have been calculated with DSAS software (Himmelstoss et al., 2024) from the original Arctic Coastal Change dataset (Nylén, 2024). Background: Copernicus Sentinel-2 NIR image from 5.8.2021.

classification. We utilize information from three Landsat sensors and multiple algorithms to enhance classification accuracy in the diverse Arctic environment. These choices mitigate issues with local illumination conditions and the low satellite data availability and quality in the Arctic in the 1980s and 1990s. Calculating post-classification composites of coastal land cover over five-year time-steps effectively reduces the impacts of local and transient conditions, such as clouds, snow, ice, suspended sediment, and the tide. Cloud computing in Google Earth Engine enables processing of the entire Arctic coast.

Wide applicability of the procedure has been pursued by utilizing three calibration sites with contrasting physical characteristics. Success in one sub-Arctic fjord coast, one glaciated coast and one low-relief permafrost coast is indicated by very high overall classification accuracy (at least 98 %). With this classification accuracy, a median shoreline error distance of the fitted shorelines is as low as 20 m in mesotidal and less than 10 m in microtidal coasts, or approximately half of the Landsat pixel size. As shoreline displacement rates calculated from our data agree well with 61 other studies across the Arctic, we are confident that the procedure performs well in most of the Arctic coastal areas.

The output of the procedure is the new Arctic Coastal Change dataset (Nylén, 2024), that can be explored through a Google Earth Engine app. We demonstrate how it unveils coastal dynamics from 1984 to 2023 at a 30-m resolution, and highlights hotspots that experience coastal erosion or accretion at a rate of more than 3 m/a. We also demonstrate how the ability to examine the data seamlessly from small to large spatial scale opens new opportunities for the study of coastal dynamics. Further exploration of the Arctic Coastal Change dataset might, however, show areas where low data availability or poor classification accuracy still prevent coastal dynamics studies. Therefore, collaborative efforts could be made to utilize and improve the Arctic Coastal Change dataset further for coastal dynamics studies at global, regional, and local scales.

Supplementary data to this article can be found online at https://doi.org/10.1016/j.rse.2025.114696.

Code and data availability

- Open asset layers in Google Earth Engine. The asset “Arctic Coastal Change” can be accessed in the Code editor with the link: https://co

de.earthengine.google.com/?asset=projects/arctic-coastal-change/assets/ArcticCoastalChange, the asset "Arctic coastal zone 2 km" with link: https://code.earthengine.google.com/?asset=projects/ee-tana-project/assets/coastalzone2km, and the asset "Arctic coastal zone 1 km" with link: https://code.earthengine.google.com/?asset=projects/ee-tana-project/assets/coastalzone1km
- Open data via Google Earth Engine App: https://arctic-coastal-change.projects.earthengine.app/view/arctic-coastal-change-viewer
- Open data via Zenodo: Nylén, T. (2024). Arctic Coastal Change (beta) [Data set]. Zenodo. doi: https://doi.org/10.5281/zenodo.13987271
- Open code for the procedure for creating the Arctic Coastal Change dataset as Supplementary material 3

CRediT authorship contribution statement

Tua Nylén: Writing – review & editing, Writing – original draft, Visualization, Validation, Software, Methodology, Investigation, Funding acquisition, Formal analysis, Data curation, Conceptualization. **Mikel Calle:** Writing – review & editing, Visualization, Methodology, Conceptualization. **Carlos Gonzales-Inca:** Writing – review & editing, Software, Methodology.

Declaration of competing interest

The authors declare no known competing financial interests or personal relationships that could have appeared to influence the work reported in this paper.

Acknowledgements

This work was funded by the Research Council of Finland – former Academy of Finland – [Tua Nylén, project ARIMPA, grant number 343338]; and the Turku Collegium for Sciences, Medicine and Technology (TCSMT) [Mikel Calle].

Data availability

Data and code are available as attachments to the paper and through public repositories referenced in the manuscript. See manuscript section "Code and data availability" for details

References

Adam, E., Mutanga, O., Odindi, J., Abdel-Rahman, E.M., 2014. Land-use/cover classification in a heterogeneous coastal landscape using RapidEye imagery: evaluating the performance of random forest and support vector machines classifiers. Int. J. Remote Sens. 35, 3440–3458. https://doi.org/10.1080/01431161.2014.903435.

AMAP, 2019. Arctic climate change update 2019: An update to key findings of snow, water, ice and permafrost in the Arctic (SWIPA) 2017. Arctic Monitoring and Assessment Programme (AMAP), Oslo, Norway, 12 pp. https://www.amap.no/documents/download/3295/inline.

Are, F., Reimnitz, E., Grigoriev, M., Hubberten, H.W., Rachold, V., 2008. The influence of cryogenic processes on the erosional Arctic shoreface. J. Coast. Res. 24, 110–121. https://doi.org/10.2112/05-0573.1.

Barbieux, K., Charitsi, A., Merminod, B., 2018. Icy lakes extraction and water-ice classification using Landsat 8 OLI multispectral data. Int. J. Remote Sens. 39, 3646–3678. https://doi.org/10.1080/01431161.2018.1447165.

Barnhart, K.R., Overeem, I., Anderson, R.S., 2014. The effect of changing sea ice on the physical vulnerability of Arctic coasts. Cryosphere 8, 1777–1799. https://doi.org/10.5194/tc-8-1777-2014.

Bartsch, A., Ley, S., Nitze, I., Pointner, G., Vieira, G., 2020. Feasibility study for the application of synthetic aperture radar for coastal erosion rate quantification across the Arctic. Front. Environ. Sci. 8, 143. https://doi.org/10.3389/fenvs.2020.00143.

Beaton, A., Whaley, R., Corston, K., Kenny, F., 2019. Identifying historic river ice breakup timing using MODIS and Google Earth Engine in support of operational flood monitoring in Northern Ontario. Remote Sens. Environ. 224, 352–364. https://doi.org/10.1016/j.rse.2019.02.011.

Bendixen, M., Kroon, A., 2017. Conceptualizing delta forms and processes in Arctic coastal environments. Earth Surf. Process. Landf. 42, 1227–1237. https://doi.org/10.1002/esp.4097.

Bishop-Taylor, R., Nanson, R., Sagar, S., Lymburner, L., 2021. Mapping Australia's dynamic coastline at mean sea level using three decades of Landsat imagery. Remote Sens. Environ. 267, 112734. https://doi.org/10.1016/j.rse.2021.112734.

Bourriquen, M., Baltzer, A., Mercier, D., Fournier, J., Pérez, L., Haquin, S., Bernard, E., Jensen, M., 2016. Coastal evolution and sedimentary mobility of Brøgger Peninsula, Northwest Spitsbergen. Polar Biol. 39, 1689–1698. https://doi.org/10.1007/s00300-016-1930-1.

Breiman, L., 2001. Random Forests. Mach. Learn. 45, 5–32. https://doi.org/10.1023/A:1010933404324.

Civco, D.L., 1993. Artificial neural networks for land-cover classification and mapping. Int. J. Geogr. Inf. Syst. 7, 173–186. https://doi.org/10.1080/02693799308901949.

Cortes, C., Vapnik, V., 1995. Support-vector networks. Mach. Learn. 20, 273–297. https://doi.org/10.1007/BF00994018.

Crist, E.P., 1985. A TM Tasseled Cap equivalent transformation for reflectance factor data. Remote Sens. Environ. 17, 301–306. https://doi.org/10.1016/0034-4257(85)90102-6.

Davy, R., Griewank, P., 2023. Arctic amplification has already peaked. Environ. Res. Lett. 18, 084003. https://doi.org/10.1088/1748-9326/ace273.

Ding, Y., Yang, X., Jin, H., Wang, Z., Liu, Y., Liu, B., Zhang, J., Liu, X., Gao, K., Meng, D., 2021. Monitoring coastline changes of the Malay Islands based on Google Earth Engine and dense time-series remote sensing images. Remote Sens. 13, 3842. https://doi.org/10.3390/rs13193842.

Donmez, C., Berberoglu, S., Cicekli, S.Y., Cilek, A., Arslan, A.N., 2021. Mapping snow cover using Landsat data: toward a fine-resolution water-resistant snow index. Meteorog. Atmos. Phys. 133, 281–294. https://doi.org/10.1007/s00703-020-00749-y.

Farquharson, L.M., Mann, D.H., Swanson, D.K., Jones, B.M., Buzard, R.M., Jordan, J.W., 2018. Temporal and spatial variability in coastline response to declining sea-ice in Northwest Alaska. Mar. Geol. 404, 71–83. https://doi.org/10.1016/j.margeo.2018.07.007.

Feyisa, G.L., Meilby, H., Fensholt, R., Proud, S.R., 2014. Automated water extraction index: a new technique for surface water mapping using Landsat imagery. Remote Sens. Environ. 140, 23–35. https://doi.org/10.1016/j.rse.2013.08.029.

Fisher, A., Flood, N., Danaher, T., 2016. Comparing Landsat water index methods for automated water classification in eastern Australia. Remote Sens. Environ. 175, 167–182. https://doi.org/10.1016/j.rse.2015.12.055.

Foody, G.M., Arora, M.K., 1997. An evaluation of some factors affecting the accuracy of classification by an artificial neural network. Int. J. Remote Sens. 18, 799–810. https://doi.org/10.1080/014311697218764.

Gibbs, A.E., Richmond, B.M., 2015. National assessment of shoreline change – historical shoreline change along the north coast of Alaska, US–Canadian border to Icy Cape. In: U.S. Geological Survey Open-File Report 1048. https://doi.org/10.3133/ofr20151048, 96 p.

Gibbs, A.E., Snyder, A.G., Richmond, B.M., 2019. National assessment of shoreline change—Historical shoreline change along the north coast of Alaska, Icy Cape to Cape Prince of Wales. In: U.S. Geological Survey Open-File Report 1146. https://doi.org/10.3133/ofr20191146, 52 p.

Gibbs, A.E., Erikson, L., Jones, B.M., Richmond, B.M., Engelstad, A.C., 2021. Seven decades of coastal change at Barter Island, Alaska: exploring the importance of waves and temperature on erosion of coastal permafrost bluffs. Remote Sens. 13, 4420. https://doi.org/10.3390/rs13214420.

Gisnås, K., Etzelmüller, B., Lussana, C., Hjort, J., Sannel, A.B.K., Isaksen, K., Westermann, S., Kuhry, P., Christiansen, H.H., Frampton, A., Åkerman, J., 2017. Permafrost map for Norway, Sweden and Finland: permafrost map for Norway, Sweden and Finland. Permafr. Periglac. Process. 28, 359–378. https://doi.org/10.1002/ppp.1922.

Günther, F., Overduin, P.P., Sandakov, A.V., Grosse, G., Grigoriev, M.N., 2013. Short- and long-term thermo-erosion of ice-rich permafrost coasts in the Laptev Sea region. Biogeosciences 10, 4297–4318. https://doi.org/10.5194/bg-10-4297-2013.

Hall, D.K., Riggs, G.A., Salomonson, V.V., 1995. Development of methods for mapping global snow cover using moderate resolution imaging spectroradiometer data. Remote Sens. Environ. 54, 127–140. https://doi.org/10.1016/0034-4257(95)00137-P.

Hijmans, R.J., Barbosa, M., Bivand, R., Brown, A., Chirico, M., Cordano, E., Dyba, K., Pebesma, E., Rowlingson, B., Sumner, M.D., 2024. terra: Spatial Data Analysis. Version 1.7.71. Available online. https://cran.r-project.org/web/packages/terra/index.html.

Himmelstoss, E.A., Henderson, R.E., Farris, A.S., Kratzmann, M.G., Bartlett, M.K., Ergul, A., McAndrews, J., Cibaj, R., Zichichi, J.L., Thieler, E.R., 2024. Digital Shoreline Analysis System Version 6.0: U.S. Geological Survey Software Release. https://doi.org/10.5066/P13WIZ8M.

Humlum, O., Instanes, A., Sollid, J.L., 2003. Permafrost in Svalbard: a review of research history, climatic background and engineering challenges. Polar Res. 22, 191–215. https://doi.org/10.3402/polar.v22i2.6455.

Irrgang, A.M., Lantuit, H., Manson, G.K., Günther, F., Grosse, G., Overduin, P.P., 2018. Variability in rates of coastal change along the Yukon coast, 1951 to 2015. J. Geophys. Res. Earth Surf. 123, 779–800. https://doi.org/10.1002/2017JF004326.

Irrgang, A.M., Lantuit, H., Gordon, R.R., Piskor, A., Manson, G.K., 2019. Impacts of past and future coastal changes on the Yukon coast – threats for cultural sites, infrastructure, and travel routes. Arct. Sci. 5, 107–126. https://doi.org/10.1139/as-2017-0041.

Irrgang, A.M., Bendixen, M., Farquharson, L.M., Baranskaya, A.V., Erikson, L.H., Gibbs, A.E., Ogorodov, S.A., Overduin, P.P., Lantuit, H., Grigoriev, M.N., Jones, B.M., 2022. Drivers, dynamics and impacts of changing Arctic coasts. Nat. Rev. Earth. Environ. 3, 39–54. https://doi.org/10.1038/s43017-021-00232-1.

Ismail, M.A., Waqas, M., Ali, A., Muzzamil, M.M., Abid, U., Zia, T., 2022. Enhanced index for water body delineation and area calculation using Google Earth Engine: a case study of the Manchar Lake. J. Water Clim. Chang. 13, 557–573. https://doi.org/10.2166/wcc.2021.282.

Jorgenson, M.T., Brown, J., 2005. Classification of the Alaskan Beaufort Sea Coast and estimation of carbon and sediment inputs from coastal erosion. Geo-Mar. Lett. 25, 69–80. https://doi.org/10.1007/s00367-004-0188-8.

Kavan, J., Strzelecki, M.C., 2023. Glacier decay boosts the formation of new Arctic coastal environments—perspectives from Svalbard. Land Degrad. Dev. 34, 3467–3474. https://doi.org/10.1002/ldr.4695.

Laengner, M.S., Siteur, K., van der Wal, D., 2019. Trends in the seaward extent of saltmarshes across Europe from long-term satellite data. Remote Sens. 11, 1653. https://doi.org/10.3390/rs11141653.

Lantuit, H., Pollard, W.H., 2008. Fifty years of coastal erosion and retrogressive thaw slump activity on Herschel Island, southern Beaufort Sea, Yukon Territory, Canada. Geomorphology 95, 84–102. https://doi.org/10.1016/j.geomorph.2006.07.040.

Lantuit, H., Overduin, P.P., Solomon, S., Mercier, D., 2010. Coastline Dynamics in Polar Systems Using Remote Sensing. Environmental Science Engineering and Technology, Nova Publishers, 174 pp., ISBN 978-1-61668-140-1.

Lantuit, H., Atkinson, D., Overduin, P.P., Grigoriew, M., Rachold, V., Grosse, G., Hubberten, H.-W., 2011. Coastal erosion dynamics on the permafrost-dominated Bykovsky Peninsula, North Siberia, 1951-2006. Polar Res. 30, 7341. https://doi.org/10.3402/polar.v30i0.7341.

Lantuit, H., Overduin, P.P., Couture, N., Wetterich, S., Are, F., Atkinson, D., Brown, J., Cherkashov, G., Drozdov, D., Forbes, D.L., Graves-Gaylord, A., Grigoriev, M.N., Hubberten, H.W., Jordan, J., Jorgenson, T., Odegard, R.S., Ogorodov, S., Pollard, W. H., Rachold, V., Sedenko, S., Solomon, S., Steenhuisen, F., Streletskaya, I., Vasiliev, A., 2012. The Arctic coastal dynamics database. A new classification scheme and statistics on arctic permafrost coastlines. Estuaries Coast 35, 383–400. https://doi.org/10.1007/s12237-010-9362-6.

Lepkowska, E., Stachnik, L., 2018. Which drivers control the suspended sediment flux in a high Arctic glacierized basin (Werenskioldbreen, Spitsbergen)? Water 10, 1408. https://doi.org/10.3390/w10101408.

Li, J., Knapp, D.E., Lyons, M., Roelfsema, C., Phinn, S., Schill, S.R., Asner, G.P., 2021a. Automated global shallow water bathymetry mapping using Google Earth Engine. Remote Sens. 13, 1469. https://doi.org/10.3390/rs13081469.

Li, J., Peng, B., Wei, Y., Ye, H., 2021b. Accurate extraction of surface water in complex environment based on Google Earth Engine and Sentinel-2. PLoS ONE 16, e0253209. https://doi.org/10.1371/journal.pone.0253209.

Li, C., Xian, G., Zhou, Q., Pengra, B.W., 2021c. A novel automatic phenology learning (APL) method of training sample selection using multiple datasets for time-series land cover mapping. Remote Sens. Environ. 266, 112670. https://doi.org/10.1016/j.rse.2021.112670.

Li, J., Ma, R., Cao, Z., Xue, K., Xiong, J., Hu, M., Feng, X., 2022a. Satellite detection of surface water extent: a review of methodology. Water 14, 1148. https://doi.org/10.3390/w14071148.

Li, K., Wang, J., Cheng, W., Wang, Y., Zhou, Y., Altansukh, O., 2022b. Deep learning empowers the Google Earth Engine for automated water extraction in the Lake Baikal Basin. Int. J. Appl. Earth Obs. Geoinf. 112, 102928. https://doi.org/10.1016/j.jag.2022.102928.

Liu, C., Hu, R., Wang, Y., Lin, H., Zeng, H., Wu, D., Liu, Z., Dai, Y., Song, X., Shao, C., 2022. Monitoring water level and volume changes of lakes and reservoirs in the Yellow River Basin using ICESat-2 laser altimetry and Google Earth Engine. J. Hydro-Environ. Res. 44, 53–64. https://doi.org/10.1016/j.jher.2022.07.005.

Luetzenburg, G., Townsend, D., Svennevig, K., Bendixen, M., Bjork, A.A., Eidam, E.F., Kroon, A., 2023. Sedimentary coastal cliff erosion in Greenland. Case Rep. Med. 128, e2022JF007026. https://doi.org/10.1029/2022JF007026.

McFeeters, S.K., 1996. The use of the Normalized Difference Water Index (NDWI) in the delineation of open water features. Int. J. Remote Sens. 17, 1425–1432. https://doi.org/10.1080/01431169608948714.

Naboureh, A., Li, A., Bian, J., Lei, G., 2023. National scale land cover classification using the semiautomatic high-quality reference sample generation (HRSG) method and an adaptive supervised classification scheme. IEEE J. Sel. Top. Appl. Earth. Obs. Remote Sens. 16, 1858–1870. https://doi.org/10.1109/JSTARS.2023.3241620.

Nielsen, D.M., Dobrynin, M., Baehr, J., Razumov, S., Grigoriev, M., 2020. Coastal erosion variability at the southern Laptev Sea linked to winter sea ice and the Arctic Oscillation. Geophys. Res. Lett. 47, e2019GL086876. https://doi.org/10.1029/2019GL086876.

Nielsen, D.M., Pieper, P., Barkhordarian, A., Overduin, P., Ilyina, T., Brovkin, V., Baehr, J., Dobrynin, M., 2022. Increase in Arctic coastal erosion and its sensitivity to warming in the twenty-first century. Nat. Clim. Chang. 12, 263–270. https://doi.org/10.1038/s41558-022-01281-0.

Nylén, T., 2024. Arctic Coastal Change (beta) [Data set]. Zenodo. https://doi.org/10.5281/zenodo.13987271.

Obu, J., Lantuit, H., Grosse, G., Günther, F., Sachs, T., Helm, V., Fritz, M., 2016. Coast erosion and mass wasting along the Canadian Beaufort Seas based on annual airborne LiDAR elevation data. Geomorphology 293, 331–346. https://doi.org/10.1016/j.geomorph.2016.02.014.

Obu, J., Westermann, S., Kääb, A., Bartsch, A., 2018. Ground temperature map, 2000-2016, northern hemisphere permafrost. Alfred Wegener Institute, Helmholtz Centre for Polar and Marine Research, Bremerhaven, Pangaea. https://doi.org/10.1594/PANGAEA.888600.

Overeem, I., Anderson, R.S., Wobus, C.W., Clow, G.D., Urban, F.E., Matell, N., 2011. Sea ice loss enhances wave action at the Arctic coast. Geophys. Res. Lett. 38, L17503. https://doi.org/10.1029/2011GL048681.

Overeem, I., Nienhuis, J.H., Piliouras, A., 2022. Ice-dominated Arctic deltas. Nat. Rev. Earth Environ. 3, 225–240. https://doi.org/10.1038/s43017-022-00268-x.

Pebesma, E., Bivand, R., Racine, E., Sumner, M., Cook, I., Keitt, T., Lovelace, R., Wickham, H., Ooms, J., Müller, K., Pedersen, T.L., Baston, D., Dunnington, D., 2024. sf: Simple Features for R. Version 1.0-19. Available online. https://cran.r-project.org/web/packages/sf/index.html.

Pekel, J.-F., Cottam, A., Gorelik, N., Belward, A.S., 2016. High-resolution mapping of global surface water and its long-term changes. Nature 540, 418–422. https://doi.org/10.1038/nature20584.

Pérez-Cutillas, P., Pérez-Navarro, A., Conesa-García, C., Zema, D.A., Amado-Álvarez, J. P., 2023. What is going on within Google Earth Engine? A systematic review and meta-analysis. Remote Sens. Appl. Soc. Environ. 29, 100907. https://doi.org/10.1016/j.rsase.2022.100907.

Philipp, M., Dietz, A., Ullmann, T., Kuenzer, C., 2023. A circum-Arctic monitoring framework for quantifying annual erosion rates of permafrost coasts. Remote Sens. 15, 818. https://doi.org/10.3390/rs15030818.

Porter, C., Morin, P., Howat, I., Noh, M.-J., Bates, B., Peterman, K., Keesey, S., Schlenk, M., Gardiner, J., Tomko, K., Willis, M., Kelleher, C., Cloutier, M., Husby, E., Foga, S., Nakamura, H., Platson, M., Wethington, M., Williamson, C., Bauer, G., Enos, J., Arnold, G., Kramer, W., Becker, P., Doshi, A., D'Souza, C., Cummens, P., Laurier, F., Bojesen, M., 2018. ArcticDEM, Version 3. https://doi.org/10.7910/DVN/OHHUKH.

Previdi, M., Smith, K.L., Polvani, L.M., 2021. Arctic amplification of climate change: a review of underlying mechanisms. Environ. Res. Lett. 16, 093003. https://doi.org/10.1088/1748-9326/ac1c29.

R Foundation for Statistical Computing, 2024. R Version 4.3.3. Available online. https://www.r-project.org/.

Radosavljevic, B., Lantuit, H., Pollard, W., Overduin, P., Couture, N., Sachs, T., Helm, V., Fritz, M., 2016. Erosion and flooding-threats to coastal infrastructure in the Arctic: a case study from Herschel Island, Yukon Territory, Canada. Estuaries Coast 39, 900–915. https://doi.org/10.1007/s12237-015-0046-0.

Rolph, R., Overduin, P.P., Ravens, T., Lantuit, H., Langer, M., 2022. ArcticBeach v1.0: a physics-based parameterization of pan-Arctic coastline erosion. Front. Earth Sci. 11, 962208. https://doi.org/10.3389/feart.2022.962208.

Rowland, J.C., Schwenk, J.P., Shelef, E., Muss, J., Ahrens, D., Stauffer, S., Pilliouras, A., Crosby, B., Chadwick, A., Douglas, M.M., Kemeny, P.C., Lamb, M.P., Li, G.K., Vulis, L., 2023. Scale-dependent influence of permafrost on riverbank erosion rates. Case Rep. Med. 128, e2023JF007101. https://doi.org/10.1029/2023JF007101.

Sandven, S., Spreen, G., Heygster, G., Girard-Ardhuin, F., Farrel, S.L., Dierking, W., Allard, R.A., 2023. Sea ice remote sensing—recent developments in methods and climate data sets. Surv. Geophys. 44, 1653–1689. https://doi.org/10.1007/s10712-023-09781-0.

Serreze, M.C., Barry, R.G., 2011. Processes and impacts of Arctic amplification: a research synthesis. Glob. Planet. Chang. 77, 85–96. https://doi.org/10.1016/j.gloplacha.2011.03.004.

Sharma, R.C., Tateishi, R., Hara, K., 2016. A new water-resistant snow index for the detection and mapping of snow cover on a global scale. Int. J. Remote Sens. 37, 2706–2723. https://doi.org/10.1080/01431161.2016.1183832.

Solomon, S.M., 2005. Spatial and temporal variability of shoreline change in the Beaufort-Mackenzie region, northwest territories, Canada. Geo-Mar. Lett. 25, 127–137. https://doi.org/10.1007/s00367-004-0194-x.

Tallentire, G.D., Shiggins, C.J., Rawlins, L.D., Evans, J., Hodgkins, R., 2023. Observing relationships between sediment-laden meltwater plumes, glacial runoff and a retreating terminus at Blomstrandbreen, Svalbard. Int. J. Remote Sens. 44, 3972–3992. https://doi.org/10.1080/01431161.2023.2229492.

Tanguy, R., Whalen, D., Prates, G., Vieira, G., 2023. Shoreline change rates and land to sea sediment and soil organic carbon transfer in eastern Parry Peninsula from 1965 to 2020 (Amundsen Gulf, Canada). Arctic Sci. 9, 506–525. https://doi.org/10.1139/as-2022-0028.

Valentin, M.M., Hogue, T.S., Hay, L.E., 2018. Hydrologic regime changes in a high-latitude glacierized watershed under future climate conditions. Water 10, 128. https://doi.org/10.3390/w10020128.

Vos, K., Splinter, K.D., Harley, M.D., Simmons, J.A., Turner, I.L., 2019a. CoastSat: a Google Earth Engine-enabled Python toolkit to extract shorelines from publicly available satellite imagery. Environ. Model. Softw. 122. https://doi.org/10.1016/j.envsoft.2019.104528. UNSP 104528.

Vos, K., Harley, M.D., Splinter, K.D., Simmons, J.A., Turner, I.L., 2019b. Sub-annual to multi-decadal shoreline variability from publicly available satellite imagery. Coast. Eng. 150, 160–174. https://doi.org/10.1016/j.coastaleng.2019.04.004.

Vos, K., Splinter, K.D., Palomar-Vázquez, J., Pardo-Pascual, J.E., Almonacid-Caballer, J., Cabezas-Rabadán, C., Kras, E.C., Luijendijk, A.P., Calkoen, F., Almeida, L.P., Pais, D., Klein, A.H.F., Mao, Y., Harris, D., Castelle, B., Buscombe, D., Vitousek, S., 2023. Benchmarking satellite-derived shoreline mapping algorithms. Commun. Earth Environ. 4, 345. https://doi.org/10.1038/s43247-023-01001-2.

Wang, J., Li, D., Cao, W., Lou, X., Shi, A., Zhang, H., 2022. Remote sensing analysis of erosion in Arctic coastal areas of Alaska and eastern Siberia. Remote Sens. 14, 589. https://doi.org/10.3390/rs14030589.

Wang, Z., Xiao, M., Nicolsky, D., Romanovsky, V., McComb, C., Farquharson, L., 2023. Arctic coastal hazard assessment considering permafrost thaw subsidence, coastal erosion, and flooding. Environ. Res. Lett. 18, 104003. https://doi.org/10.1088/1748-9326/acf4ac.

Xu, H., 2006. Modification of normalised difference water index (NDWI) to enhance open water features in remotely sensed imagery. Int. J. Remote Sens. 27, 3025–3033. https://doi.org/10.1080/01431160600589179.

Yamazaki, D., Ikeshima, D., Sosa, J., Bates, P.D., Allen, G.H., Pavelsky, T.M., 2019. MERIT hydro: a high-resolution global hydrography map based on latest topography

dataset. Water Resour. Res. 55, 5053–5073. https://doi.org/10.1029/2019WR024873.

Yan, D., Huang, C., Ma, N., Zhang, Y., 2020. Improved Landsat-based water and snow indices for extracting lake and snow cover/glacier in the Tibetan plateau. Water 12, 1339. https://doi.org/10.3390/w12051339.

Yang, X., Pavelsky, T.M., Bendezu, L.P., Zhang, S., 2022. Simple method to extract lake ice condition from Landsat images. IEEE Trans. Geosci. Remote Sens. 60 (1–10), 4202010. https://doi.org/10.1109/TGRS.2021.3088144.

Zagórski, P., Rodzik, J., Moskalik, M., Strzelecki, M.C., Lim, M., Blaszszyk, M., Prominska, A., Kruszewski, G., Styszynska, A., Malczewski, A., 2015. Multidecadal (1960-2011) shoreline changes in Isbjornhamna (Hornsund, Svalbard). Pol. Polar Res. 4, 369–390. https://doi.org/10.1515/popore−2015−0019.

Zhang, F., Yang, X., 2020. Improving land cover classification in an urbanized coastal area by random forests: the role of variable selection. Remote Sens. Environ. 251, 112105. https://doi.org/10.1016/j.rse.2020.112105.

Zhu, D., Zhou, C., Zhu, Y., Peng, B., 2022. Evolution of supraglacial lakes on Sermeq Avannarleq glacier, Greenland using Google Earth Engine. J. Hydrol. Reg. Stud. 44, 101246. https://doi.org/10.1016/j.ejrh.2022.101246.